PCCP

ROYAL SOCIETY OF CHEMISTRY

PERSPECTIVE

View Article Online
View Journal | View Issue

Cite this: *Phys. Chem. Chem. Phys.*, 2021, **23**, 27103

Polarized Raman spectroscopy in low-symmetry 2D materials: angle-resolved experiments and complex number tensor elements

Marcos A. Pimenta, *[a] Geovani C. Resende,[a] Henrique B. Ribeiro[b] and Bruno R. Carvalho *[c]

In this perspective review, we discuss the power of polarized Raman spectroscopy to study optically anisotropic 2D materials, belonging to the orthorhombic, monoclinic and triclinic crystal families. We start by showing that the polarization dependence of the peak intensities is described by the Raman tensor that is unique for each phonon mode, and then we discuss how to determine the tensor elements from the angle-resolved polarized measurements by analyzing the intensities in both the parallel- and cross-polarized scattering configurations. We present specific examples of orthorhombic black phosphorus and monoclinic 1T′-$MoTe_2$, where the Raman tensors have null elements and their principal axes coincide with the crystallographic ones, followed by a discussion on the results for triclinic ReS_2 and $ReSe_2$, where the axes of the Raman tensor do not coincide with the crystallographic axes and all elements are non-zero. We show that the Raman tensor elements are, in general, given by complex numbers and that phase differences between tensor elements are needed to describe the experimental results. We discuss the dependence of the Raman tensors on the excitation laser energy and thickness of the sample within the framework of the quantum model for the Raman intensities. We show that the wavevector dependence of the electron–phonon interaction is essential for explaining the distinct Raman tensor for each phonon mode. Finally, we close with our concluding remarks and perspectives to be explored using angle-resolved polarized Raman spectroscopy in optically anisotropic 2D materials.

Received 6th August 2021,
Accepted 15th October 2021

DOI: 10.1039/d1cp03626b

rsc.li/pccp

[a] *Departamento de Física, Universidade Federal de Minas Gerais, Belo Horizonte, Minas Gerais 30123-970, Brazil. E-mail: mpimenta@fisica.ufmg.br*
[b] *Department of Applied Physics, Stanford University, Stanford, California, 94305, USA*
[c] *Departamento de Física, Universidade Federal do Rio Grande do Norte, Natal, Rio Grande do Norte 59078-970, Brazil. E-mail: brunorc@fisica.ufrn.br*

Marcos A. Pimenta

Marcos A. Pimenta is a professor at the Department of Physics of Federal University of Minas Gerais (UFMG), Brazil, and in 1992, he created the Raman Spectroscopy Laboratory. In 1997, he started the research area of carbon nanomaterials (nanotubes and graphene) at UFMG using Raman spectroscopy. He is a member of the "Brazilian Academy of Sciences" and "The World Academy of Science (TWAS)". He got the 2013 TWAS Prize in Physics and was the president of the Brazilian Physical Society (SBF) from 2017 to 2019. Currently, he is the director of the Brazilian Institute for Science and Technology (INCT) of Carbon Nanomaterials.

Geovani C. Resende

Geovani C. Resende was born on June 21, 1993, in Três Corações city, Brazil. He obtained a bachelor's degree in Physics at Universidade Federal de Lavras, Brazil, in 2016. He received his master's degree in Physics at Universidade Federal de Minas Gerais, Brazil, in 2018, where he is currently a PhD candidate under the supervision of Prof. Dr Marcos A. Pimenta and Prof. Dr Bruno R. Carvalho. His doctoral research focuses on the electronic and vibrational properties of low symmetry 2D materials such as rhenium-type dichalcogenides by angle-resolved polarized Raman spectroscopy and resonance Raman spectroscopy.

1 Introduction

It is remarkable how the science of 2D materials has progressed since the isolation of graphene in 2004.[1] Since then, a wide family of 2D materials has been uncovered and more are yet to be discovered.[2–4] Knowledge from 3D systems has been spanned and explored in 2D materials, revealing the interesting physics limited to the atomic layer of 2D materials. There is a vast diversity of physical properties in the 2D family such as the wide range of electronic band gaps, ranging from semimetallics to insulators.[3,4] In low-symmetry 2D materials, crystalline symmetry structures play an important role since their optical, electronic and thermal properties are anisotropic in the layer plane.[5,6]

A crystal can be classified into one of the six families of symmetry:[7–9] cubic, hexagonal, tetragonal, orthorhombic, monoclinic and triclinic. This classification is based on the lengths and directions of the unitary vectors of the crystalline unit cell. A 2D material can belong to different families of symmetries. For instance, 2D transition metal dichalcogenides (TMDs) with a chemical formula MX_2 (M is the transition metal and X is the chalcogen atom) can be found in different symmetry crystalline structures depending on the type and arrangement of the metal and chalcogen atoms and on the stacking of the different layers.[10] Besides, some 2D TMDs such as MoS_2, $MoTe_2$, and WTe_2 exhibit a structural polymorphism, meaning that they can exhibit different crystalline structures. For example, the MoS_2 crystal can be arranged in hexagonal, tetragonal and orthorhombic structures.[3,5,11]

The 2D family also involves a large number of crystals made of different chemical elements and atomic structure, including h-BN, black phosphorus, transition metal monochalcogenides (MX, M = Ge, Sn; X = S, Se), transition metal trichalcogenides (MX_3, M = Ti, Zr, Hf; X = S, Se, Te), group IV–V compounds (*e.g.*, SiP, GeP, SiAs, GeAs and $GeAs_2$), group III–VI compounds (GaSe and InSe, GaTe), and ternary transition metal chalcogenides (*i.e.*, Ta_2NiS_5, $TaIrTe_4$), among others. The low-symmetry 2D materials exhibit intriguing anisotropic in-plane electrical, optical, magnetic and phonon properties,[12–22] and offer the opportunity to perform fundamental studies and be used in devices based on the anisotropic properties of electrons and phonons.

Raman spectroscopy is one of the most powerful tools to probe the fundamental properties of phonons and electrons in crystals. This technique has been widespread to characterize 3D semiconductors such as silicon,[23–25] germanium,[26,27] SiGe,[28,29] GaAs[30,31] and GaN,[32] to name a few. Based on this development, Raman spectroscopy has been spanned to study 2D materials.[33–36] Moreover, the possibility of tuning the excitation energy and performing resonant Raman spectroscopy provide further information about the electrons, phonons and their coupling in these systems.[35,37–41] Although this technique has progressed through the years, it is essential to control different parameters of the experimental setup and data analysis treatment in order to understand the basic mechanism behind the Raman scattering process. In general, one needs to pay attention to the excitation energy, number of atomic layers, experimental polarized configuration, calibration and normalization of the spectra, and interference effects on the substrate, among others. In the case of low-symmetry 2D systems, we perform angle-resolved Raman measurements by controlling and changing the direction of polarization of the incident and scattered light with respect to the crystallographic axes. We will discuss in this work how the analysis of the angle-resolved experiments provides the determination of the Raman tensor elements of the crystal.[19–21,42,43]

The Raman tensor is unique for each Raman-active mode and allows complete characterization of a given Raman peak intensity as a function of polarization of the incident and scattered light. Nowadays, there is growing interest in the study of optically anisotropic 2D materials by angle-resolved polarized Raman spectroscopy since the unusual results in layered black phosphorus (BP) were explained by Ribeiro *et al.*[21]

Henrique B. Ribeiro

Henrique B. Ribeiro is a physicist with a bachelor's degree from Universidade Federal de Minas Gerais, Brazil and has a PhD in Electrical Engineering from Mackenzie Presbyterian University, Brazil. He has been awarded the best PhD thesis in Brazil in the area of Engineering in the year 2018 by the CAPES (Federal Ministry of Education). Currently, he holds a position as a Post-Doc at Stanford University at Tony Heinz's group, researching the optical properties and light–matter interaction on 2D materials, focusing on condensed matter physics, with 17+ years of experience in optics.

Bruno R. Carvalho

Bruno R. Carvalho has a PhD in Physics from Universidade Federal de Minas Gerais, Brazil. He performed a doctoral internship at the Pennsylvania State University, USA. He has been awarded the best PhD thesis in Brazil in Physics by the CAPES (Federal Ministry of Education, 2018) and the Brazilian Physical Society (SBF, 2020). He is an affiliate member of the Brazilian Academy of Science. Currently, he holds a position as a professor of Physics at Universidade Federal do Rio Grande do Norte, Brazil. His research combines techniques from nanoscale optics to study the behavior of electrons, phonons and defects in 2D materials.

considering that the Raman tensor elements are complex numbers and that phase differences between elements are needed to fit the experimental results. Ling *et al.*[44] showed later that the tensor elements are strongly dependent on the flake thickness and the excitation energy, while Phaneuf-L'Heureux *et al.*[45] determined the Raman tensors of few-layered BP (with 2, 3, 4, and 5 layers) using angle-resolved polarized Raman spectroscopy. Mao *et al.*[46] performed polarized and resonance Raman measurements in the visible and ultraviolet energy ranges and observed from the Raman excitation profiles that the electron–phonon coupling in BP is symmetry-dependent. Also, Lin *et al.*[47] used normal and oblique laser incidences to study black phosphorus and used depth-dependent polarized results to show that the Raman response is affected by birefringence, linear dichroism and interference effects in the multilayered structures. Zhu *et al.*[48] performed angle-resolved polarized Raman measurements on both the basal and cross planes of black phosphorus and obtained the Raman tensors from the polarized spectra taken along the different crystal axes. Sriv *et al.*[49] used polarized Raman spectroscopy with six different excitation energies to study the optical phonons in layered semiconductor alloys $SnSe_{(1-x)}S_x$ and observed distinct behavior for different symmetry modes. Wang *et al.*[50] performed an angle-resolved Raman study of monoclinic 1T′-$MoTe_2$ and obtained the Raman tensors using the excitation energies of 1.96 eV and 2.33 eV. Choi *et al.*[51] investigated the angle-resolved polarized Raman response of few-layered ReS_2 and $ReSe_2$ and showed that it can distinguish the "up" and "down" orientations of the sample. Resende *et al.*[19] performed angle-dependent polarized Raman spectroscopy of single-layer triclinic $ReSe_2$, obtained the Raman tensor elements of all Raman modes, and explained the different behavior for each mode as due to the anisotropy of the electron–phonon coupling in low-symmetry 2D materials. Recently, Yu *et al.*[52] used angle-resolved polarized Raman spectroscopy to study argon ion bombarded ReS_2 samples and established the relationship between defect density and anisotropy.

There is widespread interest in unveiling the properties of optically anisotropic 2D materials and angle-resolved polarized Raman spectroscopy is a key to achieve this. In this context, we discuss in this perspective review the Raman tensor and the experimental setup used to determine its elements in low-symmetry 2D systems. We focus on the orthorhombic, monoclinic and triclinic symmetry classes discussing an example of each one of them. Interestingly, we show that some Raman modes in low-symmetry structures need to be adjusted by complex tensor elements. Therefore, a discussion of the real and imaginary parts of the Raman tensor elements is presented considering the quantum formalism for the Raman process. Finally, we shortly discuss some recent developments on the resonant angle-resolved Raman measurements in these low-symmetry structures that still need to be further explored.

1.1 The tensorial nature of the Raman intensity

When an incident laser beam hits the surface of a crystal, the electric field $\mathbf{E}^{\mathbf{i}}$ of the incident light induces a polarization vector $\mathbf{P}$ in the material medium that can be written in terms of the incident field, in the linear regime, by the expression,[53,54]

$$\mathbf{P} = \varepsilon_0 \overleftrightarrow{\chi} \cdot \mathbf{E}^{\mathbf{i}}, \tag{1}$$

where ε_0 is the electric permittivity of free space and $\overleftrightarrow{\chi}$ is the second-rank tensor electric susceptibility that accounts for the fact that the vectors $\mathbf{P}$ and $\mathbf{E}^{\mathbf{i}}$ are not necessarily parallel. The induced oscillating polarization will emit light in different directions originating the scattering of light. Most of the light is elastically scattered but a small fraction of the light is inelastically scattered due to the creation or destruction of quanta of vibrations (phonons), giving rise to the Raman scattering process. Each cartesian component χ_{ij} of the electric susceptibility tensor can be modulated by a vibrational mode μ described by the generalized normal coordinate q^{μ}. The dependence of the elements χ_{ij} on the normal coordinates q^{μ} can be expanded using a Taylor series in the normal coordinates.[54,55] The zeroth-order term of the Taylor series brings forth the Rayleigh (or elastic) scattering contribution (χ_{ij}^0) and the first-order term produces the Raman tensor elements written as,[53,54]

$$R_{ij}^{\mu} = \left(\frac{\partial \chi_{ij}}{\partial q^{\mu}}\right)\Bigg|_0, \tag{2}$$

where $i,j = x,y,z$, and the derivative of χ_{ij} is taken at the equilibrium position of the generalized coordinate ($q^{\mu} = 0$). It is important to emphasize that, even if a given element of χ_{ij} is zero by symmetry requirements, its derivative (R_{ij}^{μ}) can be different from zero.

If the incident light is polarized along the direction of the unitary vector $\hat{\mathbf{e}}^{\mathbf{i}}$, the light scattered by phonons in crystals can exhibit different polarization. If we consider only the light scattered with polarization along the unitary vector $\hat{\mathbf{e}}^{\mathbf{s}}$, as shown in Fig. 1a, the theory of light scattering shows that the Raman intensity I^{μ} of the light scattered by a phonon μ is proportional to[53,54]

$$I^{\mu} \propto \left|\hat{\mathbf{e}}^{\mathbf{i}} \cdot \overleftrightarrow{R^{\mu}} \cdot \hat{\mathbf{e}}^{\mathbf{s}}\right|^2, \tag{3}$$

where $\overleftrightarrow{R^{\mu}}$ is the second-rank Raman tensor, specific for each Raman-active phonon μ. The symbol of proportionality in eqn (3) accounts for the fact that the experimental intensity also depends on instrumental parameters (see Fig. 1b), such as the efficiency of the spectrometer, the numerical aperture of the objective, intensity of the incident light, among others. The polarization vector $\hat{\mathbf{e}}^{\mathbf{i}}$ of the incident light can be represented by a 1×3 row matrix, the polarization vector $\hat{\mathbf{e}}^{\mathbf{s}}$ of the scattered light can be represented by a 3×1 column matrix, and eqn (3) can be rewritten as:[53,54]

$$I^{\mu} \propto \left| \begin{pmatrix} e_x^{\mathrm{i}} & e_y^{\mathrm{i}} & e_z^{\mathrm{i}} \end{pmatrix} \cdot \begin{pmatrix} R_{xx}^{\mu} & R_{xy}^{\mu} & R_{xz}^{\mu} \\ R_{xy}^{\mu} & R_{yy}^{\mu} & R_{yz}^{\mu} \\ R_{xz}^{\mu} & R_{yz}^{\mu} & R_{zz}^{\mu} \end{pmatrix} \cdot \begin{pmatrix} e_x^{\mathrm{s}} \\ e_y^{\mathrm{s}} \\ e_z^{\mathrm{s}} \end{pmatrix} \right|^2. \tag{4}$$

1.2 Classical formalism and complex Raman tensor elements

The simplest model for the classical electric susceptibility considers a damped oscillating electric dipole, with a resonance

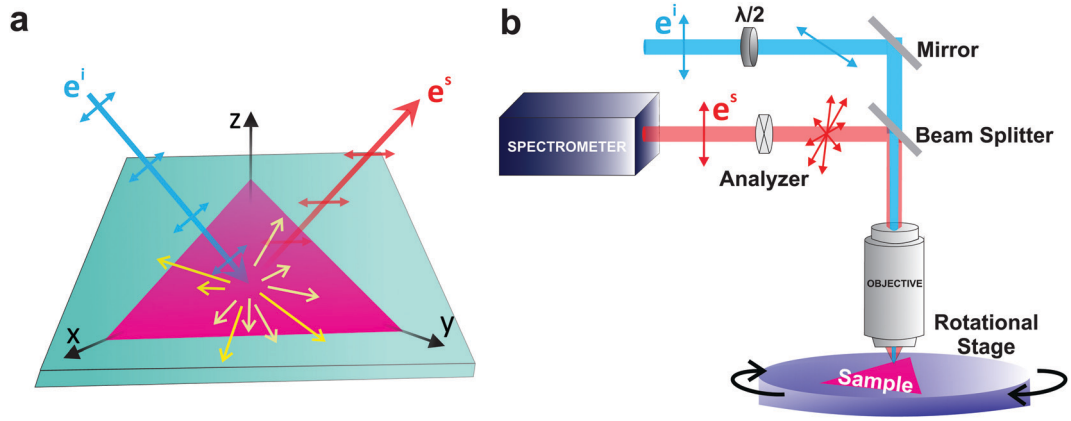

Fig. 1 Schematic of the Raman experiment setup. (a) Schematic of the light–matter interaction giving rise to the Raman scattering process. (b) Schematic of the experimental setup for a polarized Raman measurement.

frequency ω_0 and damping constant γ, forced to vibrate by the external electric field of the incident light, oscillating with a frequency ω_i. In this case, the electric susceptibility can be written as,[53,54]

$$\chi(\omega_i) = \frac{Ne^2}{m\varepsilon_0} \cdot \frac{1}{(\omega_i^2 - \omega_0^2 + i\gamma\omega_i)}, \quad (5)$$

where m and e are, respectively, the mass and charge of an electron and N is the number of dipoles per unit volume. Far away from the resonance frequencies ($\omega_i \ll \omega_0$ or $\omega_i \gg \omega_0$), the susceptibility is given by a real number since $(\omega_i^2 - \omega_0^2) \gg \gamma\omega$ and the imaginary term in the denominator can be neglected. On the other hand, we can see from eqn (5) that near the resonance the susceptibility has a complex value and can be expressed as,[53,54]

$$\chi(\omega) = \chi'(\omega) + i\chi''(\omega), \quad (6)$$

where $\chi'(\omega)$ and $\chi''(\omega)$ are the real and imaginary parts of $\chi(\omega)$. In this case, the Raman tensor elements, obtained by differentiating each component χ_{ij} of the susceptibility tensor with respect to the generalized coordinate q^μ (see eqn (2)), are also represented by complex numbers and can be written as,[53,54]

$$R_{ij}^{\mu} = R_{ij}^{\mu'} + iR_{ij}^{\mu''} = \left(\frac{\partial\chi_{ij}'}{\partial q^\mu}\right)\Big|_0 + i\left(\frac{\partial\chi_{ij}''}{\partial q^\mu}\right)\Big|_0. \quad (7)$$

The Raman tensor element can also be expressed in the complex polar plane as,[53,54]

$$R_{ij}^{\mu} = \left|R_{ij}^{\mu}\right| e^{i\phi_{ij}^{\mu}}, \quad (8)$$

where $\left|R_{ij}^{\mu}\right| = \sqrt{\left(R_{ij}^{\mu'}\right)^2 + \left(R_{ij}^{\mu''}\right)^2}$ is the modulus of the element and $\phi_{ij}^{\mu} = \arctan\left(\frac{R_{ij}^{\mu''}}{R_{ij}^{\mu'}}\right)$ is its phase.[53,54] In fact, as discussed below, we can only obtain the phase differences between the Raman tensor elements and this effect is only observed for the totally symmetric modes in low-symmetry systems. The complex nature of the Raman tensor elements has been reported in different systems of low-symmetry 2D materials[19,21,44,45,51,56–59]

For transparent 3D crystals, phase differences between tensor elements can also be associated with birefringence[60] and, in this case, the phase difference is the same for all different Raman modes. Moreover, the birefringence contribution for the phase differences is only appreciable if the material's thickness is greater than the wavelength of the incident light, and this effect is negligible in 2D systems with few atomic layers.[60] As discussed below, the observation of phase differences in single-layer low-symmetry materials is due to the resonance Raman effect, which is affected by the electron–phonon interaction, thus being specific for each Raman mode.

The electric susceptibility carries the symmetry properties of the kinetic coefficients given by $\chi_{ij}(\omega) = \chi_{ji}(\omega)$, which is derived from Onsager's principle.[54] Since the Raman tensor is given by the derivative of susceptibility with respect to the normal modes (see eqn (2)), it will also carry the property $R_{ij}(\omega) = R_{ji}(\omega)$ if the medium is non-magnetic and if we neglect the slight frequency difference between the incident and scattered photon.[54] An important consequence of the symmetry properties in the Raman tensor is the fact that the Raman tensor is not a Hermitian matrix. Therefore, we cannot diagonalize the Raman tensor when the elements are given by complex numbers. The orthogonal basis that diagonalizes the real part $R_{ij}^{\mu'}$ does not diagonalize the imaginary part $R_{ij}^{\mu''}$.

1.3 The quantum model for the Raman tensor

In this section, we will discuss the physical origin of the Raman tensor elements within the framework of the quantum model for the Raman effect, which is explained by the third-order process illustrated in Fig. 2a. In this approximation, we take explicitly into account not only the two optical transitions associated with the electron–hole creation and recombination, but also the quantum process associated with the creation or destruction of quanta of vibrations (phonons in crystals).[53,54,61]

The Raman process starts with an optical transition from the electronic initial state $|\psi_v\rangle$ in the valence band to the first intermediate state $|\psi_c\rangle$ in the conduction band; the creation (or destruction) of a vibrational quantum (phonon in a crystal)

takes the system to the second intermediate state $|\psi_{c'}\rangle$; finally, an optical transition is related to the electron–hole recombination, leaving the system in the initial electronic state $|\psi_v\rangle$ and giving rise to the scattered photon. The optical transitions are induced by the electron-radiation Hamiltonian ($H_{el\text{-}rad}$), and the creation of a phonon is induced by the electron–phonon Hamiltonian (H_{el-ph}). We will consider here the electric-dipole approximation for the electron-radiation Hamiltonian, which can be written as $H_{el\text{-}rad} = -\mathbf{d}\cdot\mathbf{E}$, where $\mathbf{d}$ is the electric-dipole operator and $\mathbf{E}$ is the electric field of the radiation, which is polarized along the direction of the unitary vector $\hat{\mathbf{e}}$.

The Raman intensity by a phonon belonging to branch μ is related to the probability of occurrence of the process illustrated in Fig. 2a, and is calculated by means of the Fermi golden rule transition probability for the third-order time-dependent perturbation process.[53,54] In this approximation, the Raman tensor element R_{ij}^{μ} depends on the excitation energy E_L according to the expression:[53,54]

$$R_{ij}^{\mu}(E_L) = \frac{1}{V}\sum_{v,c,c'}\sum_{\mathbf{k}} \frac{\langle\psi_v(\mathbf{k})|\mathbf{E}^j\cdot\mathbf{d}|\psi_{c'}(\mathbf{k})\rangle\langle\psi_{c'}(\mathbf{k})|H_{el-ph}^{\mu}|\psi_c(\mathbf{k})\rangle\langle\psi_c(\mathbf{k})|\mathbf{E}^i\cdot\mathbf{d}|\psi_v(\mathbf{k})\rangle}{[E_L - E_{cv}(\mathbf{k}) + i\Gamma_c][(E_L - E_{ph}^{\mu} - E_{c'v}(\mathbf{k}) + i\Gamma_{c'}]}, \quad (9)$$

where V is the crystal volume. The sums in eqn (9) are performed over all electronic wavevectors $\mathbf{k}$ within the first Brillouin zone and over the electronic branches v, c and c′ in the valence and conduction bands. We only consider zone-center Raman-active phonons with wavevector $\mathbf{q} = 0$. The three terms in the numerator correspond to the matrix elements of the three processes: from right to left, $\langle\psi_c(\mathbf{k})|\mathbf{E}^i\cdot\mathbf{d}|\psi_v(\mathbf{k})\rangle$ corresponds to the matrix element of the absorption of light and creation of an electron–hole pair, from the initial state $|\psi_v(\mathbf{k})\rangle$ in the valence band to the first intermediate state $|\psi_c(\mathbf{k})\rangle$ in the conduction band; $\langle\psi_{c'}(\mathbf{k})|H_{el-ph}^{\mu}|\psi_c(\mathbf{k})\rangle$ corresponds to the matrix element of the electron–phonon (el–ph) interaction that scatters the carriers from the first excited state $|\psi_c(\mathbf{k})\rangle$ to the second excited state $\left|\psi_c'(\mathbf{k})\right\rangle$ in the conduction band; and $\langle\psi_v(\mathbf{k})|\mathbf{E}^j\cdot\mathbf{d}|\psi_{c'}(\mathbf{k})\rangle$ corresponds to the matrix element of the optical transition associated with the recombination of the electron–hole pair and emission of the scattered photon. In the denominator, $E_{cv}(\mathbf{k}) = E_c(\mathbf{k}) - E_v(\mathbf{k})$ and $E_{c'v}(\mathbf{k}) = E_{c'}(\mathbf{k}) - E_v(\mathbf{k})$ are the energy differences between the valence and conduction bands at a given wavevector $\mathbf{k}$, Γ_c and $\Gamma_{c'}$ are the damping constants associated with the finite lifetime $\tau = \hbar/2\Gamma$ of the photo-excited states $|\psi_c(\mathbf{k})\rangle$ and $|\psi_{c'}(\mathbf{k})\rangle$, respectively, and E_{ph}^{μ} is the energy of phonon μ.[19] The contribution of a specific process with wavevector $\mathbf{k}$ is inversely proportional to the difference $E_L - E_{cv}(\mathbf{k})$ that appears in the denominator of eqn (9).

Let us consider the simplest particular case in eqn (9), where we ignore the two sums by restricting the optical transitions to one specific point $\mathbf{k}$ in the Brillouin zone and considering only one electronic state in the valence band ($|\psi_v(\mathbf{k})\rangle$), only one excited state in the conduction band ($|\psi_c(\mathbf{k})\rangle$), and $E_{cv}(\mathbf{k}) = \Delta E$. In this case, the phase ϕ_{ij}^{μ} of the complex tensor element R_{ij}^{μ} is given by:[19]

$$\begin{aligned}\phi_{ij}^{\mu} &= \arctan\left(\frac{R_{ij}^{\mu''}}{R_{ij}^{\mu'}}\right)\\ &= \arctan\left[\frac{-\Gamma[2(E_L - \Delta E) - E_{ph}]}{(E_L - \Delta E)(E_L - \Delta E - E_{ph}) - \Gamma^2}\right].\end{aligned} \quad (10)$$

Eqn (10) shows that the phase ϕ_{ij}^{μ} of the Raman tensor elements depends on different parameters, such as the excitation laser energy E_L, the energy gap ΔE, the damping constant Γ and the phonon frequency E_{ph}, even in the simplest situation where the two sums in eqn (9) are ignored. Fig. 2b shows the plot of ϕ_{ij}^{μ} as a function of the difference $(E_L - \Delta E)$, which is negative when the excitation energy E_L is below the bandgap energy ΔE, positive when the excitation energy is above ΔE, and zero under resonance conditions. The curves in Fig. 2b were plotted

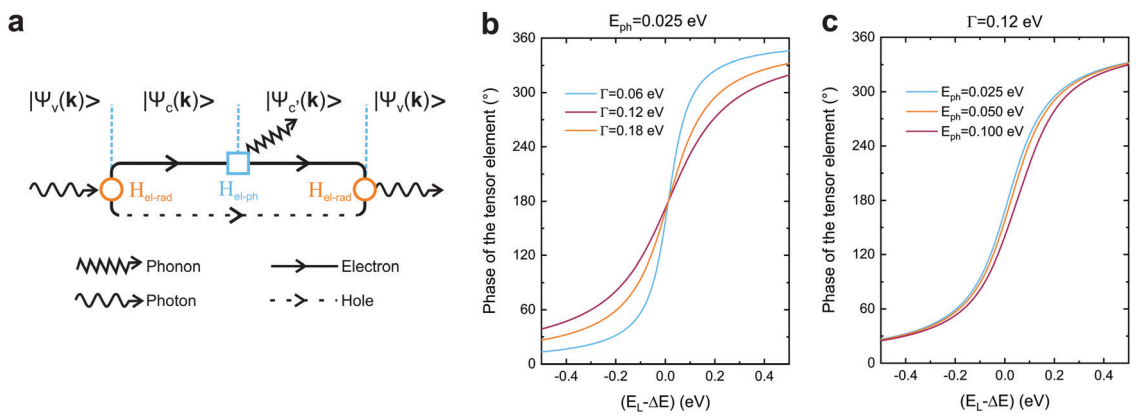

Fig. 2 Quantum framework of the Raman tensor. (a) Feynman diagram of the quantum Raman scattering process. Calculated phase of the tensor element in the quantum framework (eqn (10)) considering the fixed values of the (b) phonon energy (E_{ph} = 0.025 eV) and (c) damping (Γ = 0.12 eV).

considering three different values of Γ = 0.06 eV, 0.12 eV and 0.18 eV, which correspond to the typical values found in the literature,[20,51] and considering the phonon energy E_{ph} = 0.025 eV which corresponds to the average energy of the Raman-active phonons of $ReSe_2$. We can observe in Fig. 2b that ϕ_{ij}^{μ} tends to zero far below resonance, tends to 360° far above resonance and $\phi_{ij}^{\mu} \approx 180^{\circ}$ under resonance conditions. Fig. 2b also shows that, near resonance, the phase ϕ_{ij}^{μ} depends significantly on the value of the damping constant Γ. Fig. 2c shows the plot of ϕ_{ij}^{μ} considering three different values of the phonon energy E_{ph} = 0.025 eV, 0.050 eV and 0.100 eV and fixing the value of Γ = 0.12 eV. Notice now that the phase is only weakly dependent on the phonon energy.

1.4 Raman tensors of low-symmetry 2D materials

The most studied 2D materials, such as graphene and the semiconducting MoS_2-type transition metal dichalcogenides, belong to the hexagonal crystal family, where the 6-fold or 3-fold symmetry is perpendicular to the layer plane.[7,9] For these materials, the linear optical properties described by second-rank tensors are isotropic in the layer plane. In particular, their Raman spectrum is isotropic since the intensity of the Raman peaks do not depend on the direction of polarization of the light with respect to the crystallographic axes.[62]

In the last years, several low-symmetry 2D materials from the orthorhombic,[63–66] monoclinic[67,68] and triclinic[69,70] crystal families are being explored, and some examples are shown in Fig. 3. In these three families, the three crystallographic axes *a*, *b*, and *c* have unequal lengths. For the orthorhombic family, the three axes *a*, *b*, and *c* are perpendicular to each other.[7–9] For the monoclinic family, one axis, say the *a*-axis, is perpendicular to the *b*-axis and *c*-axis, but the *b*-axis and *c*-axis are not perpendicular to each other.[7–9] In the case of 2D monoclinic crystals, we have two possibilities: the *a*-axis can be in the plane of the layer or perpendicular to it.[7–9] For the triclinic system, the three axes are inclined at non-orthogonal (non-perpendicular) angles relative to each other.[7–9]

The orthorhombic crystal family includes the point groups D_2, C_{2v} and D_{2h}. Table 1 shows the four Raman tensors of the modes with different symmetries (different irreducible representation) for each point group of the orthorhombic crystal. Notice that in these three point groups, we have the totally symmetric representation A, A_1 or A_g for the D_2, C_{2v} and D_{2h} point groups, respectively, for which the Raman tensor is diagonal and the three elements in the diagonal are different. It also has three non-degenerate representations where the non-null elements are the off-diagonal terms *xy*, *yz* and *xz*.[7]

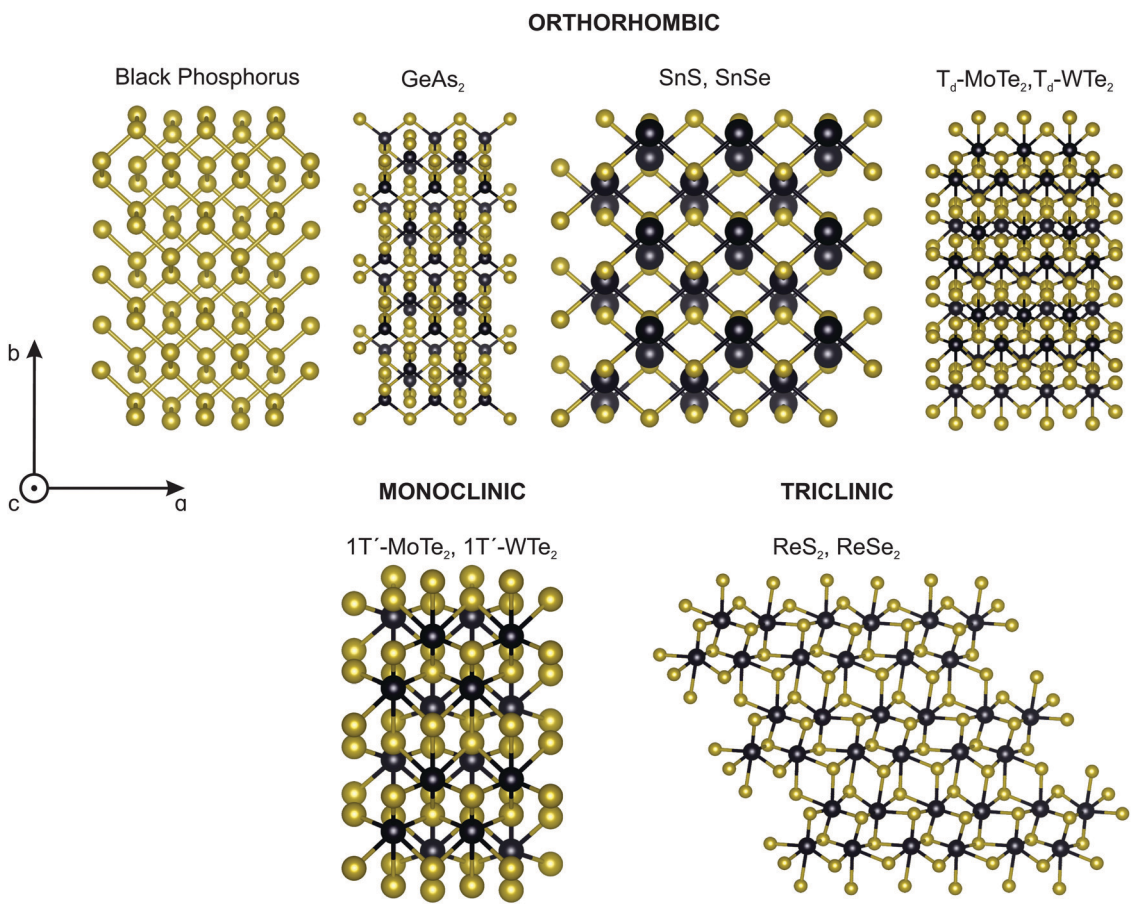

Fig. 3 Classes of low-symmetry 2D materials. Crystalline structure of the low-symmetry 2D materials: orthorhombic (*e.g.* back phosphorus, $GeAs_2$, SnS, SnSe, T_d-$MoTe_2$, T_d-WTe_2), monoclinic (*e.g.* 1T′-$MoTe_2$, 1T′-WTe_2) and triclinic (ReS_2, $ReSe_2$).

Table 1 Raman tensors for all Raman-active modes in low-symmetry crystals. For monoclinic crystal, the 2-fold axis is along the *y*-direction and the mirror *m* in the *xz* plane

Crystal symmetry	Point group	Irreducible representations of the Raman modes			
Orthorhombic	D_2	A	B_1	B_2	B_3
	C_{2v}	A_1	A_2	B_1	B_2
	D_{2h}	A_g	B_{1g}	B_{2g}	B_{3g}
	Tensor	$\begin{pmatrix} a e^{i\phi_a} & 0 & 0 \\ 0 & b e^{i\phi_b} & 0 \\ 0 & 0 & c e^{i\phi_c} \end{pmatrix}$	$\begin{pmatrix} 0 & d e^{i\phi_d} & 0 \\ d e^{i\phi_d} & 0 & 0 \\ 0 & 0 & 0 \end{pmatrix}$	$\begin{pmatrix} 0 & 0 & f e^{i\phi_f} \\ 0 & 0 & 0 \\ f e^{i\phi_f} & 0 & 0 \end{pmatrix}$	$\begin{pmatrix} 0 & 0 & 0 \\ 0 & 0 & g e^{i\phi_g} \\ 0 & g e^{i\phi_g} & 0 \end{pmatrix}$
Monoclinic	C_s	A	B		
	C_2	A_1	A_2		
	C_{2h}	A_g	B_g		
	Tensor	$\begin{pmatrix} a e^{i\phi_a} & 0 & f e^{i\phi_f} \\ 0 & b e^{i\phi_b} & 0 \\ f e^{i\phi_f} & 0 & c e^{i\phi_c} \end{pmatrix}$	$\begin{pmatrix} 0 & d e^{i\phi_d} & 0 \\ d e^{i\phi_d} & 0 & g e^{i\phi_g} \\ 0 & g e^{i\phi_g} & 0 \end{pmatrix}$		
Triclinic	C_i	A_g			
	Tensor	$\begin{pmatrix} a e^{i\phi_a} & d e^{i\phi_d} & f e^{i\phi_f} \\ d e^{i\phi_d} & b e^{i\phi_b} & g e^{i\phi_g} \\ f e^{i\phi_f} & g e^{i\phi_g} & c e^{i\phi_c} \end{pmatrix}$			

The monoclinic crystal family includes the point groups C_s, C_2 and C_{2h}. It has two Raman tensors for the modes with different symmetries (different irreducible representation) for each point group, as shown in Table 1. Here, we adopt the convention that the 2-fold axis is along the *y*-axis or the mirror plane is the *xz* plane. However, the reader should be aware that Raman tensors will be different if one adopts the convention that the 2-fold axis is along the *z*-axis or the mirror plane is the *xy* plane.[7] We can observe for the monoclinic family that the Raman tensor of the totally symmetric representation A, A_1 and A_g for the C_s, C_2 and C_{2h} point groups, respectively, is no longer a diagonal matrix, since the *xz* element is different from zero. For the other Raman tensors of the monoclinic systems, associated with the B, A_2 and B_g modes for the C_s, C_2 and C_{2h} point groups, respectively, the diagonal elements are null and the non-null elements of the matrix are the off-diagonal terms *xy* and *yz*.

The triclinic crystal family includes the point groups C_1 and C_i (or S_2) where the only non-trivial symmetry operation is the inversion center.[7] For the C_i point groups, the Raman-active modes belong to the totally symmetric A_g representation. In this case, all elements of the Raman tensor are different from zero, as shown in Table 1.

Among the vast types of low-symmetry 2D materials, this review will focus on one material of each crystal symmetry depicted in Fig. 3. In particular, we discuss the angle-resolved Raman spectra of the black phosphorus, 1T′-$MoTe_2$ and $ReSe_2$ in the following sections.

2 Angle-resolved polarized Raman spectra

2.1 Orthorhombic crystal: black phosphorus

Black phosphorus (BP) consists of atomically thin layers of phosphorus atoms covalently bonded to the neighboring atoms, forming a puckered honeycomb structure.[71,72] The atomic structure of a monolayer BP exhibits an orthorhombic symmetry, which belongs to the D_{2h} point (space group *Pmna*).[73,74] By definition of the crystallographic axes of the BP structure,[75] the *a* and *c* axes are, respectively, along the zigzag and armchair directions, and the *b* axis is perpendicular to the layer plane. A BP structure can be stacked in different manners,[76–78] with the AB-stacking configuration being the most stable.[22,77,79,80] The atomic structure of the bulk BP stacked in the AB configuration belongs to the D_{2h} point group, but to the face-centered space group *Cmce*.[81,82] In this case, the face-centered unit cell contains 8 atoms, but the primitive cell of the AB-stacked bulk BP only contains 4 atoms.[81,83]

Group theory predicts 3 acoustic and 9 optical phonon branches for the monolayer and bulk BP, and the irreducible representations at the Brillouin zone center (Γ point) are[8,9] $\Gamma = 2A_g \oplus B_{1g} \oplus B_{2g} \oplus 2B_{3g} \oplus A_u \oplus 2B_{1u} \oplus 2B_{2u} \oplus B_{3u}$, where we considered the definition of the crystallographic axes aforementioned. Only the $2A_g \oplus B_{1g} \oplus B_{2g} \oplus 2B_{3g}$ phonons are Raman active.[22,84–87] In a conventional back-scattering Raman configuration, where the light polarization is in the *xz* plane, only the A_g^1, A_g^2 and B_{2g} modes are observed in the Raman spectrum, as shown in Fig. 4. The B_{1g} and B_{3g} only appear in the spectrum where the incident light has a polarization component along the *y*-axis.[21]

The angular dependence of the polarized Raman spectra can be performed by fixing the analyzer either parallel or perpendicular to the fixed incident polarization while the sample is rotated (see Fig. 1b).[19,21,88] The polarized Raman spectra of a bulk BP in the XX and XZ configurations are shown in Fig. 4a and b. Notice that the intensities of the A_g^1, B_{2g} and A_g^2 modes vary in these configurations. Fig. 4c and d show the angle-resolved polarized Raman map excited with a 2.33 eV laser energy in the parallel and crossed polarized configurations,

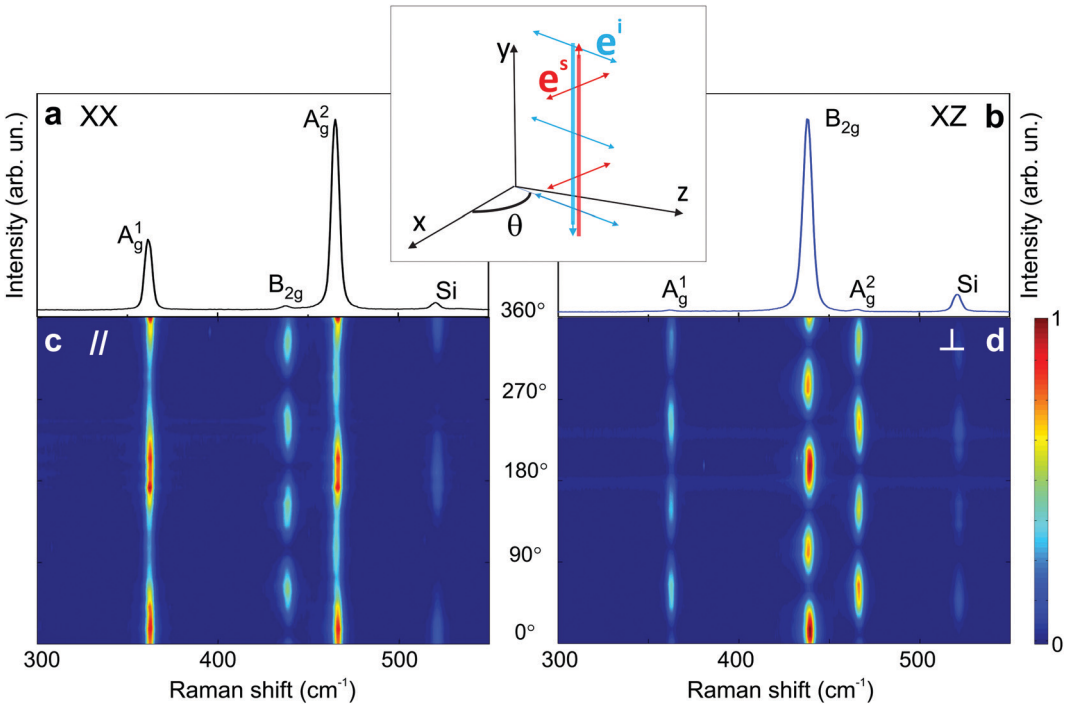

Fig. 4 Characteristic Raman spectrum of the orthorhombic black phosphorus. Polarized Raman spectra in the (a) *XX* and (b) *XZ* configurations. Typical angle-resolved Raman map of BP in the (c) parallel (∥) and (d) crossed (⊥) configurations. These results are from an exfoliated BP flake. Adapted with permission from ref. 21.

respectively. Here, the angle θ is between the incident light polarization and the *x*-axis, as shown in the inset of Fig. 4. The intensities of the A_g^1, B_{2g} and A_g^2 modes are given by the colorbar.[21]

The angular dependence of the Raman peak intensities shown in Fig. 4c and d can be explained considering eqn (3), the Raman tensors R^{A_g} and $R^{B_{2g}}$ of the different modes, and the polarization vectors $\hat{\mathbf{e}}^i$ and $\hat{\mathbf{e}}^s$ of the incident and scattered light, respectively. The results shown in Fig. 4 were collected in the back-scattering configuration where the beam of the incident laser was along the *y* axis of bulk BP.[21] Therefore, we only need to consider the Raman tensor elements related to the *x* and *z* axes, provided by the first and third rows (or columns) of the Raman tensors shown in Table 1. Thus, we consider the 2 × 2 blocks of the A_g and B_{2g} modes in the *xz* plane, given by,[53,54]

$$R^{A_g} = \begin{pmatrix} ae^{i\phi_a} & 0 \\ 0 & ce^{i\phi_c} \end{pmatrix}, R^{B_{2g}} = \begin{pmatrix} 0 & fe^{i\phi_f} \\ fe^{i\phi_f} & 0 \end{pmatrix}, \quad (11)$$

where $a, c, f > 0$ are the moduli of the tensor elements. The incident light can be polarized in the *xz* plane, and the incident polarization unit vector $\hat{\mathbf{e}}^i$ can be expressed by a 1 × 2 matrix, $\hat{\mathbf{e}}^i = (\cos\theta, \sin\theta)$, with θ being the angle between $\hat{\mathbf{e}}^i$ and the *x*-axis (see the inset of Fig. 4b). We also need to fix the scattered light polarization, described by the unit vector $\hat{\mathbf{e}}^s$, to determine the Raman tensors elements. The polarized geometries of the unit vector $\hat{\mathbf{e}}^s$ are normally parallel and crossed (or perpendicular) to $\hat{\mathbf{e}}^i$, and the unit vector $\hat{\mathbf{e}}^s$ can be expressed by a 2 × 1 matrix: $\hat{\mathbf{e}}^s = \begin{pmatrix} \cos\theta \\ \sin\theta \end{pmatrix}$ for the parallel configuration, and $\hat{\mathbf{e}}^s = \begin{pmatrix} -\sin\theta \\ \cos\theta \end{pmatrix}$ for the crossed configuration.

By introducing the expressions of the incident and scattered polarized unit vectors and the Raman tensor in eqn (3), we can obtain the angular dependence intensity equations for the A_g and B_{2g} modes in the parallel (∥) and crossed (⊥) configurations, $I_{\parallel}^{A_g}(\theta)$, $I_{\perp}^{A_g}(\theta)$, $I_{\parallel}^{B_{2g}}(\theta)$, and $I_{\perp}^{B_{2g}}(\theta)$. As an example, we calculated the expression of the angular intensity of the A_g mode in the crossed configuration,[53,54]

$$I_{\perp}^{A_g}(\theta) \propto \left| (\cos\theta \quad \sin\theta) \cdot \begin{pmatrix} ae^{i\phi_a} & 0 \\ 0 & ce^{i\phi_c} \end{pmatrix} \cdot \begin{pmatrix} -\sin\theta \\ \cos\theta \end{pmatrix} \right|^2 \quad (12a)$$

$$= \left[(a - c\cos\phi_{ac})^2 + c^2 \sin^2\phi_{ac} \right] \sin^2\theta \cos^2\theta, \quad (12b)$$

where $\phi_{ac} = (\phi_c - \phi_a)$ is the relative phase between the *c* and *a* components of the A_g tensor. Therefore, using the same procedure, the angular dependence of the Raman scattering intensities of the A_g and B_{2g} modes in the parallel and crossed polarization configurations are given by,[53,54]

$$I_{\parallel}^{A_g}(\theta) = (a\cos^2\theta + c\cos\phi_{ac}\sin^2\theta)^2 + c^2\sin^4\theta\sin^2\phi_{ac}, \quad (13a)$$

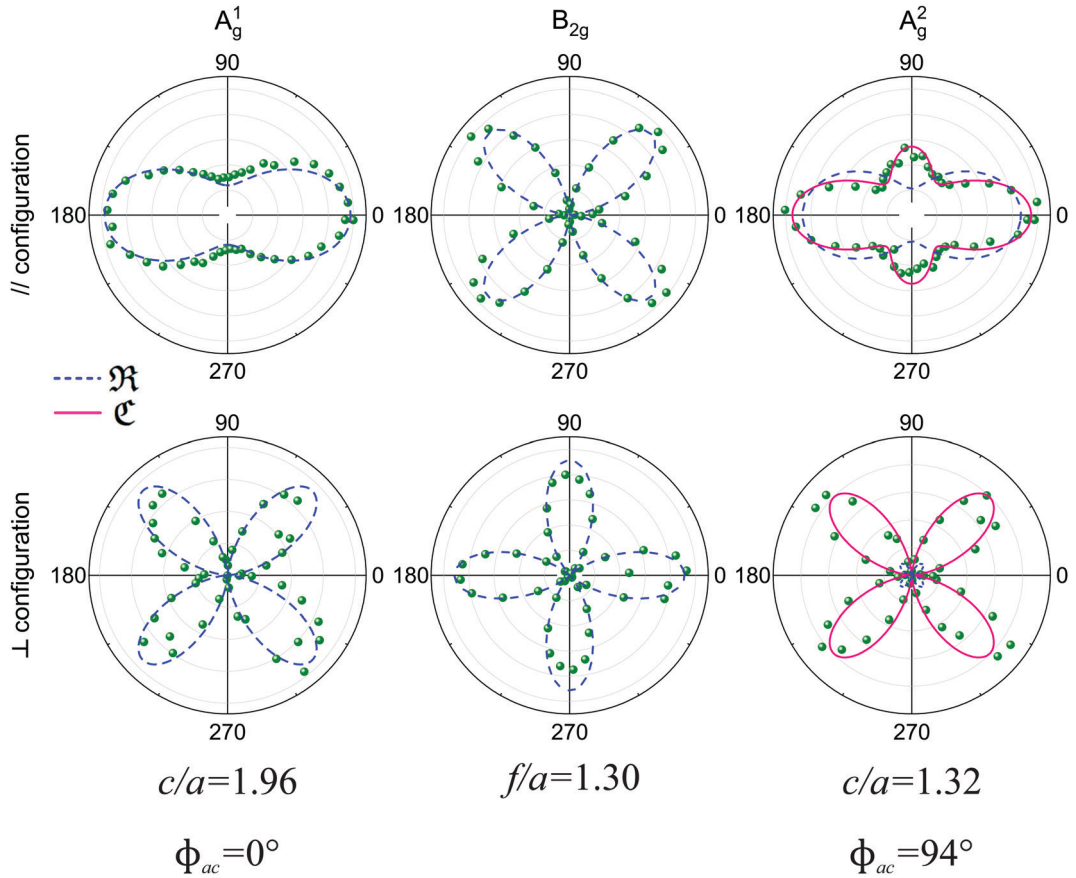

Fig. 5 Angle-resolved Raman response of the orthorhombic black phosphorus. Angular dependence of the intensities of the A_g^1, B_{2g} and A_g^2 modes in the parallel (∥, top panel) and crossed (⊥, bottom panel) polarization configurations for an exfoliated BP flake for an excitation energy of 2.33 eV. The corresponding tensor element ratios and phase differences extracted from the fitting process are also shown. Adapted with permission from ref. 21.

$$I_{\perp}^{A_g}(\theta) = [(a - c\cos\phi_{ac})^2 + c^2\sin^2\phi_{ac}]\sin^2\theta\cos^2\theta, \quad (13b)$$

$$I_{\parallel}^{B_{2g}}(\theta) = (2f\sin\theta\cos\theta)^2, \quad (13c)$$

$$I_{\perp}^{B_{2g}}(\theta) = (f\cos 2\theta)^2. \quad (13d)$$

An important result is that the phase ϕ_f of the non-diagonal term of the B_{2g} tensor disappears when the square modulus is taken in eqn (5). Therefore, the information regarding the phase ϕ_f of the non-diagonal of the B_{2g} matrix tensor is lost in the analysis of the angle-resolved polarized Raman experiments in orthorhombic materials.[21] The same behavior is observed for the other non-diagonal B_{1g} and B_{3g} tensors. Thus, information about Raman tensor phases in orthorhombic materials can only be obtained through the angle-resolved results of the totally symmetric A_g modes. Moreover, the analysis of the experimental result allows us to determine only the difference of the diagonal elements phases $\phi_{ac} = (\phi_c - \phi_a)$.[21]

To determine the Raman tensors of the A_g^1, B_{2g} and A_g^2 modes of BP, we need to fit the angular dependence of $I_{\parallel}(\theta)$ and $I_{\perp}(\theta)$, shown in Fig. 5, with the same set of elements for each mode. The curves in Fig. 5 represent the best fit of $I_{\parallel}$ and $I_{\perp}$ with the same set of tensor elements, respectively. The dashed blue curves represent the best fit considering only real numbers for the tensor elements, corresponding to the situation where the phase difference ϕ_{ac} is zero ($\sin\phi_{ac} = 0$ and $\cos\phi_{ac} = 1$ in eqn (13a) and (13b)). Note from Fig. 5 that for the totally symmetric A_g modes, the angular dependence of $I_{\parallel}$ exhibits a 2-fold symmetry (with periodicity of 180°), with the maxima at 0° and 180° and the minima (or secondary maxima) at 90° and 270°.[21] The reason for this behavior is the fact that $c/a < 1$, and the opposite trend will occur when $c/a > 1$. On the other hand, the angular dependence of the cross-polarized intensity $I_{\perp}$ for the totally symmetric A_g modes exhibits a 4-fold symmetry (with periodicity of 90°), with maxima at 45°, 135°, 225° and 315°. For the B_{2g}-symmetry mode, its angular dependence in both $I_{\parallel}$ and $I_{\perp}$ exhibits a 4-fold symmetry, but the maxima of the $I_{\parallel}$ are at 45°, 135°, 225° and 315°, whereas the maxima of the $I_{\perp}$ are at 0°, 90°, 180° and 270°. The angular dependence behavior shown in Fig. 5 is characteristic of the orthorhombic symmetry of the BP crystal, where the principal axes of the real part of the susceptibility and Raman tensors are necessarily along the crystallographic axes.[7,53]

The experimental results of the B_{2g} mode shown in Fig. 5 in both $I_{\parallel}$ and $I_{\perp}$ can be fitted by real number tensor elements, as expected from eqn (13c) and (13d) and shown by the dashed

blue curves in Fig. 5. The results of $I_{\parallel}$ and $I_{\perp}$ for the A_g^1 mode shown in Fig. 5 can also be fitted by real number elements, since $\phi_{ac} = 0$. However, for the A_g^2 mode, the fit by real number elements fails dramatically, as shown by the dashed blue curves in Fig. 5. In this case, a phase difference ϕ_{ac} is needed to fit the angular dependence of both $I_{\parallel}$ and $I_{\perp}$, as shown by the solid pink curves for the A_g^2 mode in Fig. 5. The important consequences of introducing the phase difference ϕ_{ac} are the appearance of a secondary maxima in the angular dependence of $I_{\parallel}$, at 90° and 270°, and the significant enhancement of the intensities of $I_{\perp}$ at 45°, 135°, 225° and 315°.

The angle-polarized Raman results mentioned above show the importance of properly measuring and analysing the angle-resolved intensities in the parallel ($I_{\parallel}$) and crossed ($I_{\perp}$) configurations. The determination of tensor elements only with the analysis of the parallel polarized intensities ($I_{\parallel}$) can lead to misleading values for the Raman tensor elements.

2.2 Monoclinic crystals: 1T′-$MoTe_2$ type compounds

In monoclinic crystals, one crystallographic axis is perpendicular to two other axes, which are not perpendicular to each other.[7,9] The point groups that belong to the monoclinic system are C_2 (2), C_{1h} (m) and C_{2h} (2/m). In the case of 2D monoclinic crystals, there are two possibilities: in one category of 2D monoclinic crystals, the 2-fold axis is perpendicular to the layer plane and in other case, the 2-fold axis is along the layer plane. Here, we discuss the monoclinic 1T′ structure of TMDs which includes $MoTe_2$ and WTe_2 and that belongs to the second category mentioned above.

The monoclinic 1T′ structure of $MoTe_2$ corresponds to a distortion of the 1T structure of TMD compounds, which has hexagonal symmetry.[11] Differently from the MoS_2-type TMDs, where the layer formed by the S (chalcogens) atoms, above and below the layer composed of Mo (transition metal) atoms, are on the top of each other, in the 1T structure the chalcogens are not on the top of each other, but instead rotated by 60°. The 1T′-$MoTe_2$ structure belongs to the C_{2h} point group and to the $P12_1/m$ 1 space group. We have written the full notation for the space group to show that the 2-fold axis is along the y-direction. The notation 2_1 shows that the 2-fold axis is a screw axis.

We need to pay attention when analysing character tables and Raman tensors for monoclinic crystals, since the 2-fold axis in 1T′-$MoTe_2$ is normally considered to be the y-axis and many textbooks assume that the 2-fold axis in monoclinic systems is along the z-direction. Thus, considering that the 2-fold axis is along the y-direction, the A_g symmetry Raman modes are expected to be observed in the XX, YY, ZZ and XZ polarized spectra, whereas the B_g modes appear in the XY and YZ spectra. Using the conventional back-scattering configuration with the incident light is along the z-axis, the A_g modes appear in the XX and YY parallel polarized spectra and the B_g modes in the crossed polarized XY spectrum.[59,66,89]

The unit cell of a monolayer 1T′-$MoTe_2$ contains 6 atoms, while in its bulk form the unit cell contains 12 atoms.[68] According to group theory predictions, 9 modes are expected to appear in the first-order Raman spectrum of monolayer 1T′-$MoTe_2$ (6 A_g modes and 3 B_g modes). For bulk 1T′-$MoTe_2$, 12 A_g modes and 6 B_g modes are predicted to appear in the first-order Raman spectra.[68]

Fig. 6 shows the angle-resolved polarized Raman map of a 4 nm thick sample of 1T′-$MoTe_2$ in the parallel ($\parallel$) and crossed ($\perp$) configurations.[50] The polar plots of the intensities $I_{\parallel}$ and $I_{\perp}$ for some Raman modes are shown in Fig. 6c. Note that in the parallel configuration, the A_g^2, A_g^3, A_g^4 and A_g^5 modes have a 2-fold symmetry with their maxima at 90° and 270°. The A_g^1 and A_g^6 modes also exhibit a 2-fold symmetry, but their maxima are at 0° and 180°. In the case of the B_g modes, they show a 4-fold symmetry on both configurations similarly to the B_{2g} modes in orthorhombic BP (see Fig. 5).

The Raman intensity for the A_g and B_g modes in the parallel and crossed polarization configurations is given by eqn (3) and the Raman tensor in Table 1 resulting in,[53,54]

$$I_{\parallel}^{A_g}(\theta) = (a\cos^2\theta + b\cos\phi_{ab}\sin^2\theta)^2 + c^2\sin^4\theta\sin^2\phi_{ab}, \quad (14a)$$

$$I_{\perp}^{A_g}(\theta) = [(a - b\cos\phi_{ab})^2 + b^2\sin^2\phi_{ab}]\sin^2\theta\cos^2\theta, \quad (14b)$$

$$I_{\parallel}^{B_g}(\theta) = (2d\sin\theta\cos\theta)^2, \quad (14c)$$

$$I_{\perp}^{B_g}(\theta) = (d\cos 2\theta)^2. \quad (14d)$$

The polar plots shown in Fig. 6 were fitted using complex Raman tensor elements,[50] as shown by the black and red curves for the parallel and crossed configurations, respectively. We can note that the fitting of the A_g^2, A_g^3, and A_g^4 modes in the parallel configuration exhibits secondary maxima and resembles the A_g^2 mode of BP shown in Fig. 5. We can conclude that the behavior of angle-resolved Raman measurements in 2D monoclinic crystals where the 2-fold axis is in the layer plane is similar to that in orthorhombic crystals. The angle-resolved Raman behavior of 2D monoclinic crystals where the 2-fold axis is perpendicular to the plane will be similar to that in triclinic systems, which will be discussed in the next subsection.

2.3 Triclinic crystal: rhenium diselenide

The atomic structures of monolayer and bulk rhenium diselenide ($ReSe_2$) belong to the triclinic C_i point group, which only has the identity and the inversion center as symmetry operations.[70,90] In both cases, the unit cell has 12 atoms (4 rhenium and 8 selenium atoms) and exhibits diamond-shaped rhenium–rhenium bonds forming quasi-one-dimensional chains.[57,70] Group theory predicts 3 acoustic branches and 33 optical branches in the phonon dispersion of $ReSe_2$, and 18 zone-center modes with the A_g symmetry are Raman active.[57,70] Fig. 7a shows the Raman spectrum of the monolayer $ReSe_2$, where the experimental data correspond to the blue dots and the orange curves represent the fit by Lorentzian curves, which allows us to identify the 18 A_g predicted Raman modes.[19]

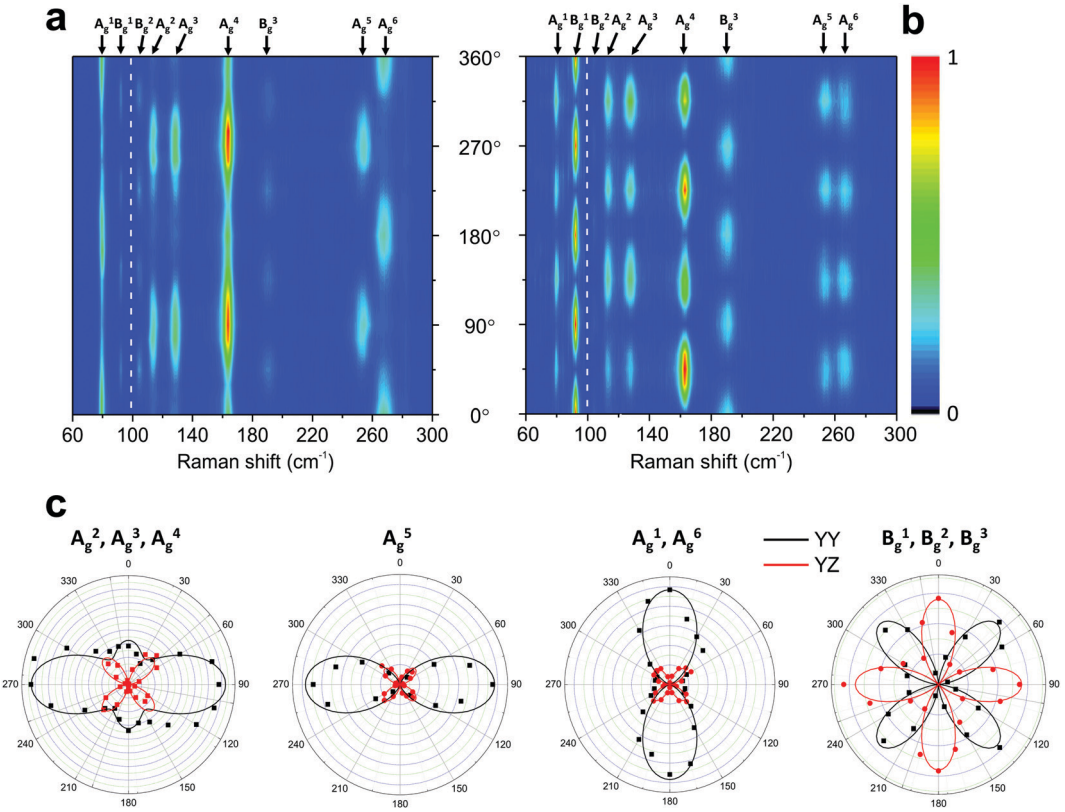

Fig. 6 Typical angle-resolved Raman map of a monoclinic 1T′-$MoTe_2$. Raman map in the (a) parallel (∥) and (b) crossed (⊥) polarization configurations. (c) Angular dependence of the intensities of the 1T′-$MoTe_2$ peaks shown in (a) and (b). The angle-resolved Raman map was constructed using two excitation energies: 1.96 eV (below 100 cm^{-1}) and 2.33 nm (above 100 cm^{-1}). Adapted with permission from ref. 50.

Fig. 7b and c show the angular dependence of the polarized Raman spectra of the monolayer $ReSe_2$ in the parallel (∥) and crossed (⊥) configurations, respectively, where the angle θ is between the incident light polarization $\hat{\mathbf{e}}^{i}$ and the x-axis. The striking difference of these maps with respect to those of the orthorhombic and monoclinic crystals shown in Fig. 4 and 6 is the fact that the maxima and minima of both $I_{\parallel}$ and $I_{\perp}$ in Fig. 7b and c are not at fixed angles. Instead, they are at general angles which, in turn, are different for each mode.[19] In fact, this is a consequence of the low-symmetry of the crystal, since all elements of the Raman tensor in triclinic systems are non-null.[7] When the tensor has both diagonal and non-diagonal terms if written in the crystallographic axes of the systems, we can diagonalize the real part of the tensor and determine the principal axes. In this case, the principal axes are not along the crystallographic axes and, in turn, are at different angles for the different Raman modes.[19]

To analyze the results shown in Fig. 7, we need to introduce in eqn (3) the Raman tensor R^{A_g} of triclinic crystals and the polarization vectors $\hat{\mathbf{e}}^{i}$ and $\hat{\mathbf{e}}^{s}$ of the incident and scattered light, respectively. In the back-scattering geometry used in ref. 19, only the components of the first 2 × 2 block matrix associated with the x and y coordinates need to be considered since the laser beam is along the z-direction. The term $ae^{i\phi_a}$ can be put in evidence outside the matrix and we can write the Raman tensor considering only the 2 × 2 block in the xy plane as:[53,54]

$$R^{A_g} = \begin{pmatrix} ae^{i\phi_a} & de^{i\phi_d} \\ de^{i\phi_d} & be^{i\phi_b} \end{pmatrix} = ae^{i\phi_a}\begin{pmatrix} 1 & (d/a)e^{i(\phi_d-\phi_a)} \\ (d/a)e^{i(\phi_d-\phi_a)} & (b/a)e^{i(\phi_b-\phi_a)} \end{pmatrix}, \quad (15)$$

where a, b, $d > 0$ are the absolute values and ϕ_a, ϕ_b, ϕ_d are the phases of the complex tensor elements. When the matrix above is introduced in eqn (3), the phase term $e^{i\phi_a}$ disappears when the square modulus of the expression is taken. Therefore, we cannot obtain the phases ϕ_a, ϕ_b, and ϕ_d of the tensor elements in an angle-resolved polarized Raman experiment, but only the phase differences $(\phi_b - \phi_a)$ and $(\phi_d - \phi_a)$.[19,20] Moreover, since we are not measuring the absolute values of the Raman intensity, which would require the control of different parameters in the experimental setup, we cannot obtain the absolute values of a, b and d, but only the ratios b/a and d/a.

The polarized Raman intensities for the A_g modes in triclinic systems in the parallel ($I_{\parallel}$) and crossed ($I_{\perp}$) configurations, obtained by introducing the tensor in eqn (15) into eqn (3), are given by:[53,54]

$$I_{\parallel}(\theta) \propto a^2\cos^4\theta + b^2\sin^4\theta + (d\sin 2\theta)^2 + \sin 2\theta\left(\frac{1}{2}ab\cos\phi_{ab}\right.$$
$$\left. \times \sin 2\theta - 2ad\cos\phi_{ad}\cos^2\theta - 2bd\cos(\phi_{ad}-\phi_{ab})\sin^2\theta\right) \quad (16a)$$

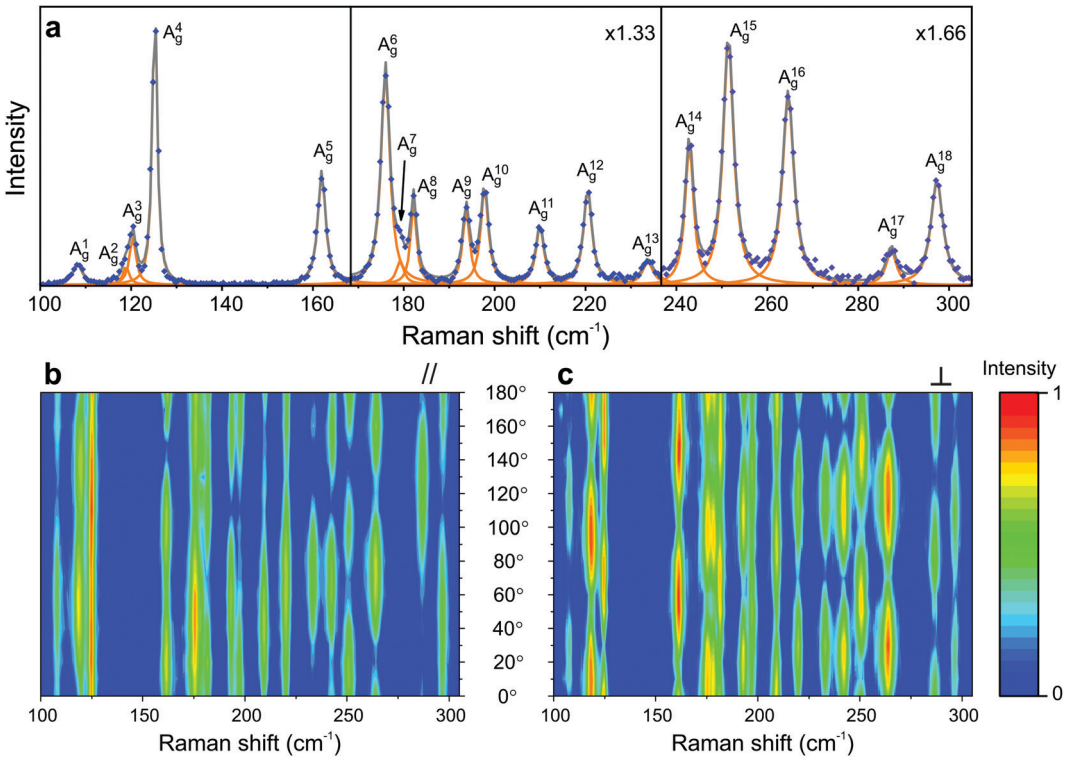

Fig. 7 Characteristic Raman spectrum of the triclinic $ReSe_2$; (a) Raman spectrum of a monolayer $ReSe_2$ showing the 18 A_g modes predicted by group theory. Typical angle-resolved Raman map of $ReSe_2$ in the (b) parallel (||) and (c) crossed (⊥) configurations. The spectra and mapping were collected with a 2.33 eV laser energy. Adapted with permission from ref. 19.

$$I_{\perp}(\theta) \propto \left(a^2 + b^2 - 2ab\cos\phi_{ab}\right)\left(\frac{1}{2}\sin 2\theta\right)^2 + (d\cos 2\theta)^2 - \frac{1}{2}\sin 4\theta(bd\cos(\phi_{ad} - \phi_{ab}) - ad\cos\phi_{ad}) \quad (16b)$$

where θ is the angle between the polarization vector $\hat{\mathbf{e}}^{i}$ and the x-axis, and $\phi_{ab} = (\phi_b - \phi_a)$ and $\phi_{ad} = (\phi_d - \phi_a)$ are the phase differences of the elements of the tensor.[19]

Another interesting difference between orthorhombic and triclinic systems is related to the phases of Raman tensor elements, which are necessary to explain the experimental angular dependence of $I_{\parallel}$ and $I_{\perp}$ of the A_g symmetry modes.[19] As shown in section 2.1, for orthorhombic crystals, we need to consider the phase difference $\phi_{ac} = (\phi_c - \phi_a)$ between the diagonal elements of the tensor. However, for triclinic systems, we need to consider not only the phase difference $\phi_{ab} = (\phi_b - \phi_a)$ between the diagonal elements but also the phase difference between the non-diagonal and one diagonal element, $\phi_{ad} = (\phi_d - \phi_a)$.

Fig. 8 shows examples of the angular dependence of $I_{\parallel}(\theta)$ and $I_{\perp}(\theta)$ for six different A_g Raman modes of the monolayer $ReSe_2$. The dots represent the experimental data, and the curves correspond to the best fitting by eqn (7) considering real and complex tensor elements. The dashed blue curves represent the best fit considering only real tensor elements, where the phase differences ϕ_{ab} and ϕ_{ad} are 0° or 180°. The solid pink curves in Fig. 8 represent the best fit of $I_{\parallel}$ and $I_{\perp}$ when the tensor elements are complex numbers and the phase differences ϕ_{ab} and ϕ_{ad} are included.

We can observe in Fig. 8 that the angular dependence of $I_{\parallel}$ and $I_{\perp}$ of modes A_g^7, A_g^{13} and A_g^{15} can be fitted when the elements of the Raman tensors are real numbers, since the phase differences are 0° or 180°. However, for modes A_g^4, A_g^5 and A_g^9, the disagreement between the experimental data and the fitting considering real numbers is evident, especially in the case of the crossed ($I_{\perp}$) polarization results. The predicted minima of $I_{\perp}$ considering real elements are zero, but the experimental results show that the minima of $I_{\perp}$ are not zero. The effect of the phase of the tensor element also appears in the angular dependence of the parallel polarized intensity $I_{\parallel}$. We conclude that the angular dependence of 2D triclinic crystals can only be explained if we consider that the tensor elements are complex numbers and if we introduce the phase differences ϕ_{ab} and ϕ_{ad} in eqn (16a) and (16b) to fit the angle-resolved polarized intensities.

Another important aspect of the Raman spectra in triclinic systems is the fact that they are different in the two different faces of the 2D sample. In fact, the atomic structure of ReX_2 (X = S or Se) crystals lacks a rotation by π around any axis parallel to the layer plane, which results in two distinct

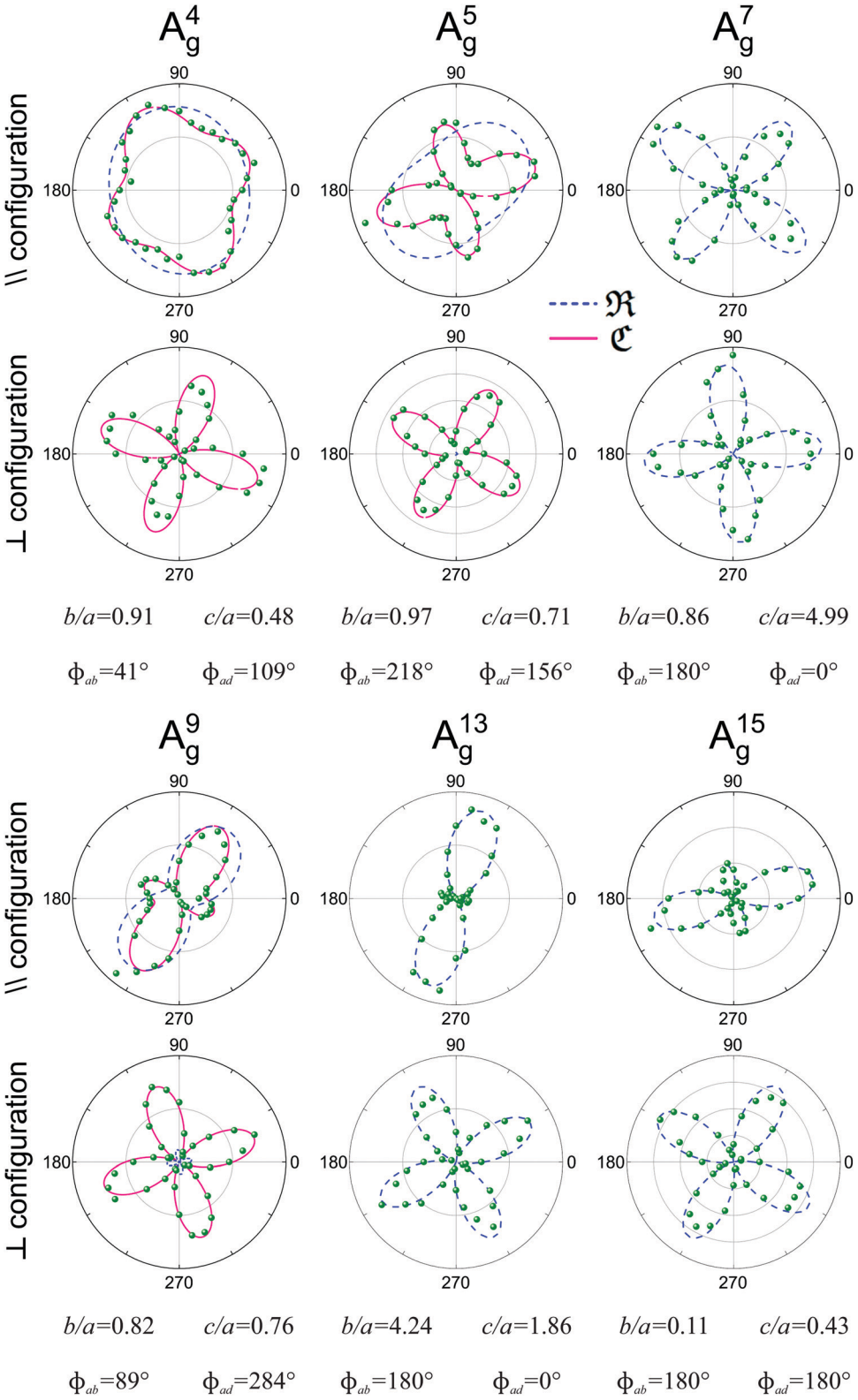

Fig. 8 Typical Raman polar plots of a monolayer triclinic $ReSe_2$. Angular dependence of the intensities of 6 A_g modes in the parallel (∥) and crossed (⊥) configurations for an exfoliated monolayer $ReSe_2$ collected using an excitation energy of 2.33 eV. The corresponding tensor element ratios and phase differences extracted from the fitting process are also shown. Adapted with permission from ref. 19.

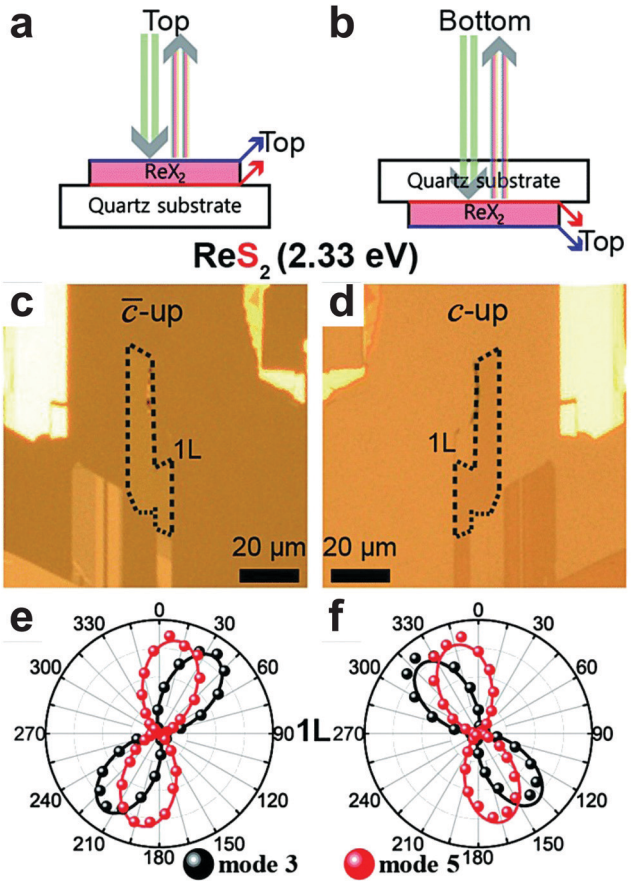

Fig. 9 The flipping-like a coin behavior in triclinic 2D materials. Scheme of the laser beam to probe the vertical orientation in triclinic ReX_2 (X = S or Se) in the (a) "up" and (b) "down" sample's orientation. Optical images of the monolayer ReS_2 in the (c) "up" and (d) "down" orientation show in (a and b). Angle-polarized Raman response of modes 3 and 5 of monolayer ReS_2 in the (e) "up" and (f) "down" orientations. Adapted with permission from ref. 51.

vertical orientations, "up" or "down".[51,70,91] Hart *et al.* showed that it is possible to experimentally obtain crystals in these orientations in a controlled manner through mechanical exfoliation.[91] They also have shown that for a rotation by π around the *y*-axis changes the sign of the *xy* and *yz* elements of the Raman tensors. Choi *et al.* performed angle-polarized Raman measurements on ReS_2 and $ReSe_2$ exfoliated crystals placed on a transparent quartz substrate in both "up" and "down" orientations,[51] by turning the substrate upside down as schematized in Fig. 9a and b and shown in Fig. 9c and d. The ReS_2 samples were excited by a 2.33 eV laser line. Fig. 9c and d show that the upside turn of the substrate is a π rotation around the 0° direction pointed in the optical images. Their angle-resolved polarized results in the "up" and "down" orientation are shown in Fig. 9e and f, respectively. As one can observe, for phonon modes of ReS_2 labelled as mode 3 and mode 5[51] the polar plots in Fig. 9e are rotations of the polar plots in Fig. 9f around the vertical direction. The same trend was observed for $ReSe_2$ samples.[51]

3 Resonant Raman effects in low-symmetry 2D materials

3.1 Black phosphorus

Further investigation about the anisotropic Raman response of low-symmetry 2D materials has been provided by the combination of polarized Raman with resonant Raman spectroscopies. The latter has shown to be a powerful tool to probe the electronic structure, excitons and electron–phonon interactions in 2D materials, such as twisted-bilayer graphene,[39] $MoTe_2$,[40] and MoS_2,[37,38] among others.[34,35,62,92–95]

In few-layered black phosphorus, Mao *et al.* observed symmetry-dependent electron–phonon couplings in the experimental Raman excitation profiles of the different modes, which were supported by density functional theory calculations.[46] It was shown in this work that, despite the fact that both A_g modes in black phosphorus exhibit in-plane and out-of-plane components, the "in-plane" vibrational A_g^2 mode exhibits a stronger resonance in the visible range than the "out-of-plane" A_g^1 mode, as shown in Fig. 10a and b. For excitation energies in the visible range, the A_g^2 mode has a strong resonance behavior in the armchair and zigzag directions (see Fig. 10a and b), whereas the A_g^1 mode exhibits a weak resonance in both directions, except when excited at the 2.70 eV and with polarization in the zigzag direction (see Fig. 10a and b).[46] In addition, it was observed that, for excitation energies in the 2.60–2.73 eV range, the Raman response of the A_g^1 mode is more intense in the zigzag than in the armchair direction as shown in Fig. 10c–f, despite the fact that the absorption is higher in the armchair direction in this energy range.[46] This result is a strong indication that the electron–phonon coupling can be more relevant for the enhancement of Raman response than the intrinsic resonance effect in this range of excitation energies. Moreover, the difference in the resonance behavior for these two A_g modes increases in the UV region, where the intensity of A_g^1 becomes very weak.

These results can be understood considering the symmetry dependence of the exciton–phonon coupling, as observed in semiconducting 2D MoS_2[38] and $MoSe_2$.[41] In the black phosphorus case, although both A_g modes share the same irreducible representation, the atoms vibrate along the armchair direction in the A_g^2 mode, which therefore couples more efficiently with the optical transition for electric dipole along the same direction (see Fig. 10c). On the other hand, the A_g^1 mode involves the vibration of atoms mainly in the out-of-plane direction and, therefore, does not exhibit such efficient coupling (see Fig. 10d). Similarly, the weak resonance for both A_g modes in the zigzag direction can be attributed to the fact that few-layered BP is almost transparent for visible light polarized in this direction.[46] It is worth noting that few-layer black phosphorus absorbs UV light in the zigzag direction and, therefore, the stronger signal observed for the A_g^2 mode suggests that the in-plane mode also couples more efficiently with in-plane electric dipole transition.

3.2 ReS_2 and $ReSe_2$ triclinic crystals

Fig. 8 shows that the orientation and shape of the polar plots of the angular-resolved dependence of the polarized Raman

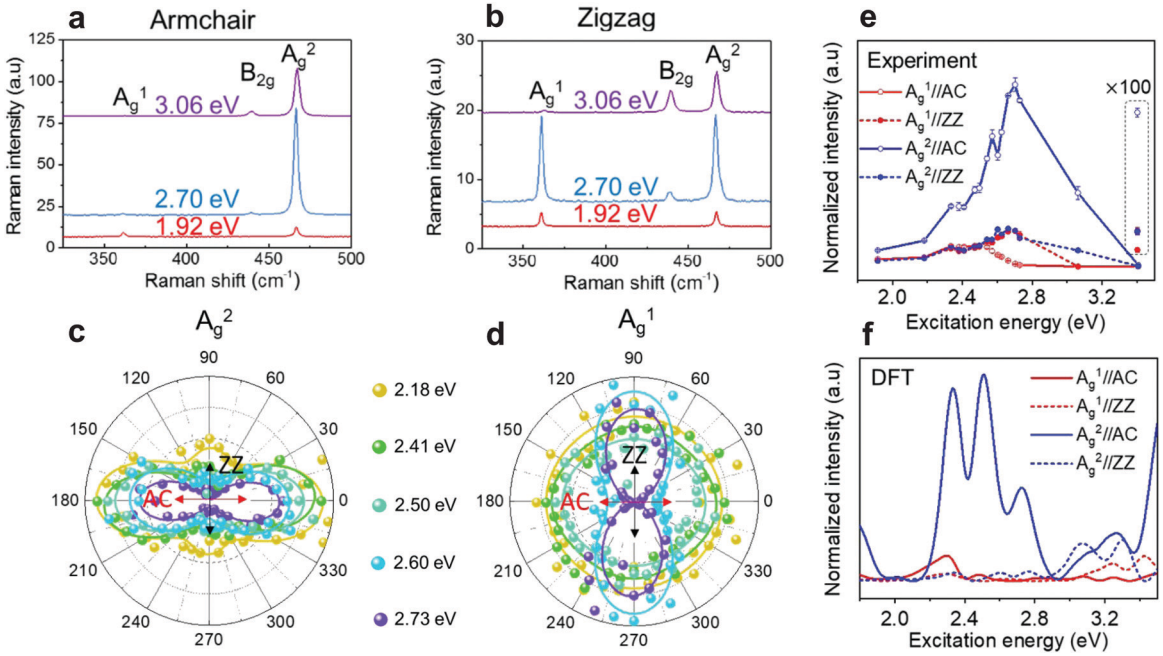

Fig. 10 Resonant Raman response of an orthorhombic black phosphorus. Resonant Raman spectra of a 7.7 nm BP flake (~14 layers) for the excitation energies of 1.92 eV, 2.70 eV and 3.06 eV along the (a) armchair and (b) zigzag directions. Resonant angle-resolved Raman results for different excitation energies of the (c) A_g^2 and (d) A_g^1 modes for a ~10 nm BP flake. (e) Experimental and (f) calculated Raman excitation profiles of A_g^1 (red curves) and A_g^2 (blue curves) along the armchair (AC) and zigzag (ZZ) directions. Adapted with permission from ref. 46.

intensities in monolayer $ReSe_2$ are distinct for each one of the 18 Raman modes.[19,51] This is a consequence to the fact that all elements of the Raman tensor are non-null and, therefore, the presence of diagonal and non-diagonal terms makes the orientation of the tensors independent on the crystalline axes. In this section, we show that the orientation and shape of the polar plots for the Raman modes of the ReX_2 (X = S or Se) also depend on the excitation laser energy and on the number of layers of the 2D materials.

Choi *et al.* performed a systematic angle-resolved polarized Raman study of ReS_2 and $ReSe_2$ samples with one, two and three layers (1L, 2L and 3L) recorded with different excitation laser energies.[51] Fig. 11 shows the Raman intensity polar plots of the first five A_g modes in the monolayer (1L), bilayer (2L) and trilayer (3L) $ReSe_2$, where the red, green and blue dots correspond to the intensities recorded, respectively, with the 1.96, 2.33 and 2.81 eV excitation laser energies in the "up" orientation of the sample.[51] Note in the first row of Fig. 11 that both the orientation and shape of the polar plots of the 1L $ReSe_2$ are distinct for each excitation energy. This result shows that the Raman tensor elements and the ratio between the non-diagonal to diagonal terms in triclinic systems depend on the excitation energy used to perform the angle-resolved experiments and also on the number of layers of the sample.

In a recent work, Resende *et al.* reported an angle-resolved polarized Raman study in 1L and bulk $ReSe_2$ for the excitation energies of 1.92 eV and 2.34 eV, in order to investigate the effects of dimensionality and excitation energy on the Raman tensors of $ReSe_2$.[20] The Raman tensors for all 18 A_g modes were obtained considering a simultaneous fitting of the angular dependence in the parallel ($I_\parallel$) and cross ($I_\perp$) polarized intensities. It was observed that, as expected for a triclinic system excited near resonance conditions, the tensor elements are in general complex numbers and the angular dependence of the polarized Raman intensities is only fitted by considering phase differences between tensor elements.[20] Fig. 12a–d show, respectively, the Raman tensor element ratio (b/a and d/a) and the phase differences for the 1.92 eV and 2.34 eV laser energies for all 18 A_g modes of a monolayer $ReSe_2$. We can observe that the phase differences of the 18 A_g modes in 1L $ReSe_2$ vary between 0 and 180°, which in turn are different for the 1.92 eV and 2.34 eV excitation energies (see Fig. 12). In most cases, both the tensor elements and phases vary with the change of the excitation energy. For the tensor elements, the b/a ratio for the 2.34 eV laser energy is less scattered than the data for the 1.92 eV, and the c/a ratio is less scattered for both laser energies. Similar behavior can be observed for the phase differences. It was demonstrated in this work that the complex Raman tensor elements contain the contribution of the scattering process of a unique $ReSe_2$ layer and other contribution related to the interference of the scattered light coming from the different layers of the material.[20]

McCreary *et al.* investigated the resonant Raman behavior of rhenium disulfide (ReS_2) for different number of layers (1L, 2L, 4L and bulk) using four excitation energies (1.58, 1.96, 2.41 and 2.54 eV).[56] It was shown that most of the modes in ReS_2 exhibit a maximum intensity peak when excited with the 1.58 eV energy, which is close to the excitonic transition for 2L, 4L and bulk, but a low-intensity response in the Raman spectrum of 1L ReS_2 collected at the 1.58 eV energy.[56] The peaks that

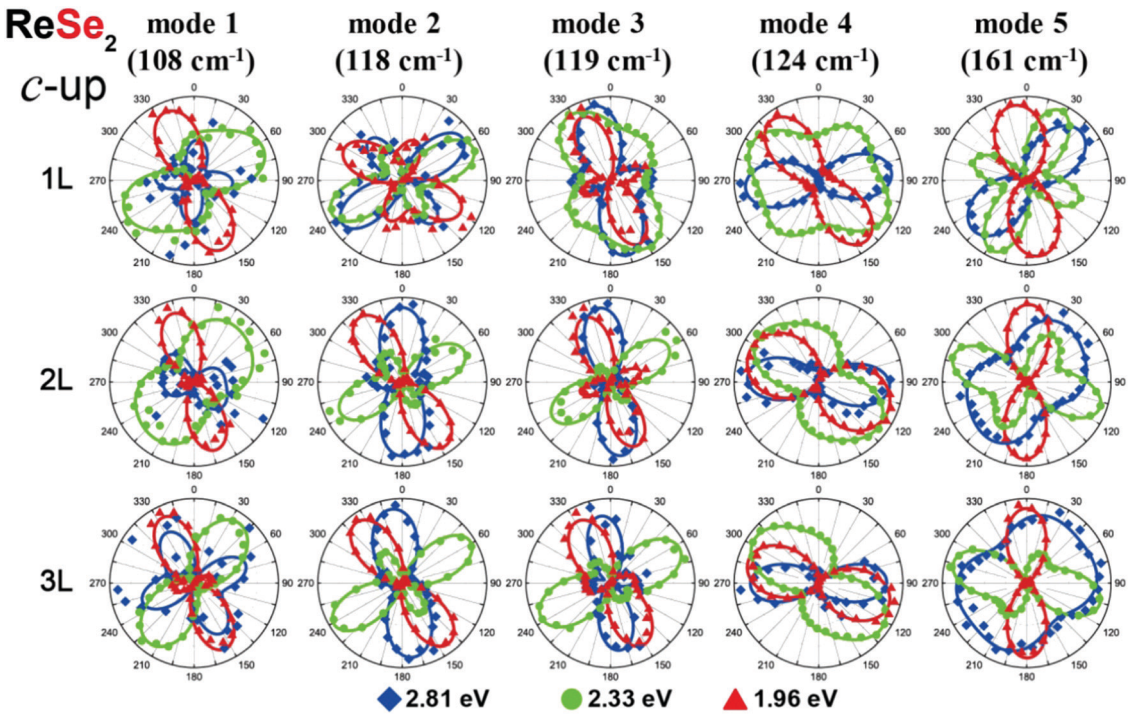

Fig. 11 Resonant Raman response of a triclinic $ReSe_2$. Resonant angle-resolved Raman dependence of some modes of a few-layered $ReSe_2$ in the "up" orientation for excitation energies of 1.96, 2.33, and 2.81 eV, respectively. Adapted with permission from ref. 51.

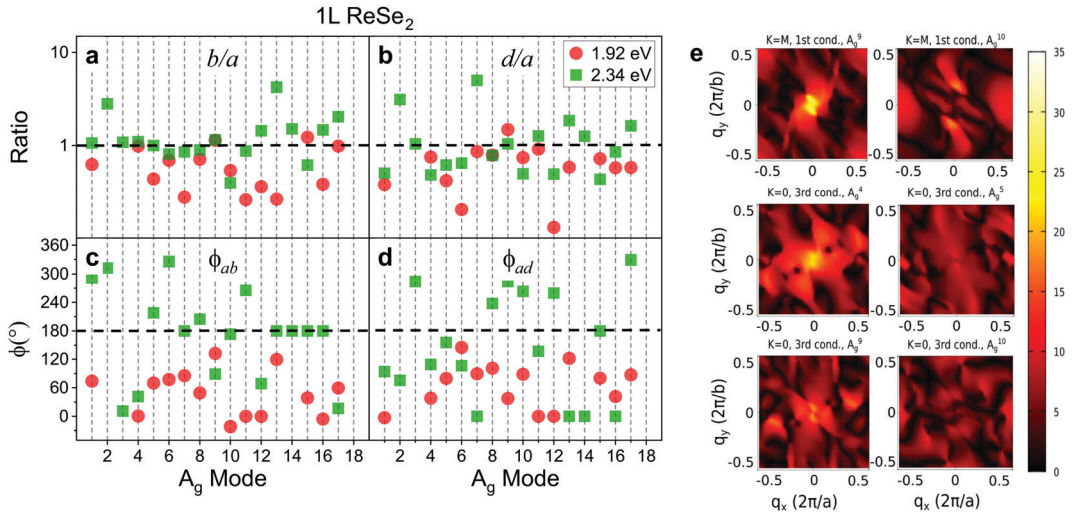

Fig. 12 Raman tensor elements and phase differences of a monolayer $ReSe_2$. (a and b) Ratio values of the Raman tensor elements (in a logarithmic scale) and (c and d) the phase differences for all 18 A_g of a monolayer $ReSe_2$ for 1.92 eV and 2.34 eV excitation laser energies. (e) Calculated electron–phonon couplings for A_g^9 and A_g^{10} between the lowest conduction band electronic states at the *M* point and for A_g^4, A_g^5, A_g^9, and A_g^{10} between the third lowest conduction band electronic stated at the **G** point. The color-bar scale is in units of meV. Images (a–d) were adapted with permission from ref. 20 and image (e) was adapted with permission from ref. 19.

exhibited the highest intensity are those associated with the *S*-atoms vibrations (*e.g.* A_g^2, A_g^3, A_g^{12}, A_g^{15}, A_g^{16} and A_g^{18} modes). A large intensity enhancement was observed for the modes related to the out-of-plane vibration of the Re atoms for the 1.58 eV excitation energy. However, the modes corresponding to the in-plane vibrations of the Re atoms (*e.g.* A_g^6 and A_g^7 modes) show a significant enhancement only when excited at 1.96 eV.[56] The A_g^1 and A_g^8 modes, which are also related to Re in-plane vibrations, also present considerable intensity change but only for the 2L and 4L ReS_2 samples.[56]

3.3 Origin of the complex Raman tensors and electron–phonon coupling

In this section, we will discuss the physical origin of the Raman tensor elements and the phase differences between tensor elements observed in low-symmetry crystals. We show that the dependence of the tensor elements on the laser excitation energy and on the number of layers in 2D materials is a consequence of the resonant Raman effect that occurs when the photons of the Raman process (absorption or emission) are in resonance with the optical transitions of the material.

According to the expression for the Raman tensor elemens R_{ij}^{μ} shown in eqn (9), the modulus of the tensor elements depends on the three matrix elements in the numerator and on the two resonant terms in the denominator of the expression. On the other hand, the phase ϕ_{ij}^{μ} depends only on the terms in the denominator of eqn (9). Eqn (10) corresponds to the simplest expression for the phase ϕ_{ij}^{μ}, where we ignore the sums in eqn (9), and considers only two electronic energy levels in the valence and conduction bands. The strong dependence of the phase ϕ_{ij}^{μ} on the difference $(E_L - \Delta E)$ observed in Fig. 2b explains why the modulus and phase differences of the Raman tensor elements observed in low-symmetry 2D materials depend on the laser excitation energy. It also explains why the Raman tensor elements are different in single-layered, few layered and bulk 2D materials, since the electronic band structure and excitonic optical transitions depend on the number of layers and are distinct in the single-layer, few-layers and bulk regimes.

The observed results that each Raman mode exhibits a distinct angle-resolved polarized Raman spectra and a specific Raman tensor in low-symmetry 2D materials cannot be explained by the weak dependence of ϕ_{ij}^{μ} on the phonon frequency E_{ph} shown in Fig. 2b. In fact, the distinct and particular behavior of each Raman mode is due to the dependence of the electron–phonon matrix element $\langle \psi_{c'}(\mathbf{k}) | H_{el\text{-}ph}^{\mu} | \psi_{c}(\mathbf{k}) \rangle$ on the wavevector $\mathbf{k}$ of the electronic state. Despite the fact that only $\mathbf{q} \sim 0$ phonons are involved in first-order Raman scattering, the vertical optical transitions occur for all electronic wavevectors $\mathbf{k}$ within the Brillouin zone. Fig. 12e shows the maps of the electron–phonon coupling as a function of the wavevector $\mathbf{k}$ over the entire Brillouin zone for six different normal modes of $ReSe_2$.[19] We can clearly observe in Fig. 12e that the maxima of the electron–phonon coupling for each Raman mode occur at different wavevectors $\mathbf{k}$ in the BZ. Therefore, the dependence of the electron–phonon matrix elements on $\mathbf{k}$ explains the distinct values of the modulus and phases of the Raman tensor elements for each Raman mode.

In summary, we can observe from eqn (9) that the modulus of the Raman tensor elements depends on the three matrix elements in the numerator of the expression, but the phases depend only on the terms in the denominator of eqn (10). For the two optical transitions, we need to take into account the electric fields $\mathbf{E}$ of the incident and scattered radiation polarized along the directions $\hat{\mathbf{e}}^{\mathbf{i}}$ and $\hat{\mathbf{e}}^{\mathbf{j}}$, respectively, and the matrix elements of the electric dipole operator $\mathbf{d}$ between states in the valence and conduction bands. The sum in eqn (9) is performed over all wavevectors $\mathbf{k}$ within the first Brillouin zone, and the contribution of a specific process with wavevector $\mathbf{k}$ for the Raman intensity is directly proportional to the three matrix elements in the numerator of eqn (9) and inversely proportional to the difference $[E_i - E_{cv}(\mathbf{k})]$ that appears in the denominator of eqn (9). We thus need to consider the dependence of all terms of eqn (9) on the wavevector $\mathbf{k}$ to explain the specific angular dependence for each Raman mode.

4 Concluding remarks

In the emerging field of 2D materials, new systems with different chemical elements and atomic structures are being extensively produced and studied. Raman spectroscopy is a fundamental experimental tool to investigate 2D materials that has been widespread in graphene and spanned to other 2D compounds such as the transition metal dichalcogenides. Raman spectra provide information about different physical properties of the sample, such as disorder, strain, presence of charges, number of layers, atomic structure of edges, and stacking arrangement, among others. Moreover, the possibility of using multiple excitation laser energies allows investigating the physics of excitons predominant in 2D layered materials and the electron–phonon interactions. In high symmetry 2D materials, such as graphene and MoS_2, the intensity of the Raman peaks does not depend on the direction of the incident light polarization with respect to the crystallographic axes. However, in low-symmetry 2D systems belonging to the orthorhombic, monoclinic and triclinic crystal families, the intensity of each Raman mode depends on the polarization of the incident light with respect to the crystallographic axes of the material. The anisotropy on the Raman response in low-symmetry materials is described by the Raman tensor, which is specific for each Raman-active mode.

In this perspective review, we started discussing the tensorial nature of the Raman response in crystals and the angle-resolved polarized Raman experiments, where one can vary the angle between the light polarization with respect to the crystalline axes. We have shown that it is of utmost importance to use a polarizer/analyzer to control the polarization of the scattered light to correctly determine the values of the Raman tensor elements from the analysis of the angle-resolved polarized intensities. In the most common configurations for the polarized Raman experiments, the polarization of the incident light can be parallel ($\parallel$) or perpendicular ($\perp$) to the polarization of the scattered light. The tensor elements are obtained by fitting the angular dependence of the parallel ($I_{\parallel}$) and crossed ($I_{\perp}$) Raman intensities with the same set of tensor elements for each mode. We have shown that the directions of the maxima and minima of $I_{\parallel}$ for orthorhombic systems are along the crystalline axes and the maxima of $I_{\perp}$ make an angle of 45° with respect to the crystalline axes. In monoclinic 1T′-$MoTe_2$, the angle-resolved experiments are similar to the orthorhombic case since the 2-fold symmetry axis is in the layer plane. For triclinic systems, the maxima in the angular dependence

of $I_{\parallel}$ and $I_{\perp}$ are at general orientations and distinct for each Raman mode. This behavior is a consequence of the fact that all elements of the Raman tensor in triclinic systems are different from zero. The co-existence of diagonal and non-diagonal elements in the Raman tensors makes the directions of the maxima of $I_{\parallel}$ and $I_{\perp}$ independent on the directions of the crystalline axes.

Most of the low-symmetry 2D materials studied so far, such as black-phosphorus and $MoTe_2$, are semiconducting and the energies of the photons normally used in Raman spectroscopy are above their energy band gaps. Therefore, their Raman intensities are enhanced by the resonances of the photons with higher energy electronic (or excitonic) transitions. In this case, the Raman tensor elements are complex numbers, with a modulus and a phase. Information about the phases of the Raman tensor elements is lost in higher symmetry materials but is preserved in the case of low-symmetry materials. However, we can only obtain values of the phase differences between the elements of the Raman tensor from the analysis of the angle-resolved experiments. It was shown that the unusual angular dependence of the polarized spectra of black-phosphorus can be nicely explained by considering the phase difference between the two diagonal elements of the tensor associated with the totally symmetric A_g^2 modes. In the case of triclinic and semiconducting materials such and ReS_2 and $ReSe_2$, it was shown that the complex nature of the tensor elements is observed for the majority of the modes, and phase differences between diagonal elements and between diagonal and non-diagonal elements are needed to fit the experimental angular dependence of $I_{\parallel}$ and $I_{\perp}$.

We have analyzed the results for the Raman tensors in low symmetry 2D materials within the framework of the quantum model for the Raman process, in which we consider explicitly not only the two optical transitions associated with the incident and scattered photons but also the matrix element of the electron–phonon process. For the determination of the Raman tensor, we need to sum the contribution over all $\mathbf{k}$ points in the Brillouin zone. Due to the resonance effect, the contribution of each $\mathbf{k}$-vector for the Raman tensor element will be inversely proportional to the difference $E_L - \Delta E(\mathbf{k})$ between the laser energy and the bandgap at this $\mathbf{k}$ point. Moreover, we also need to consider the contribution of the electron–phonon matrix element and its dependence on the wavevector $\mathbf{k}$ for the Raman tensor. The fact that the Raman tensor is different for each mode is a clear evidence that the dependence of the electron–phonon matrix elements on $\mathbf{k}$ plays a fundamental role to describe the angle-resolved polarized Raman spectra in low-symmetry 2D materials.

Finally, the possibility of performing measurements in samples of low-symmetry 2D materials with a different number of layers (1L, 2L, 3L and up to bulk) will allow the distinction of the contributions for the Raman tensor from a single atomic layer and from the light scattered by different layers of a multi-layered sample. Although there are some recent studies on the resonant Raman effect in low-symmetry 2D materials, most of the reports have used only a few laser excitation energies. A detailed multiple energy excitation Raman study, where we can tune the excitation laser energy across the excitonic transitions, will be needed to unveil the electron–phonon or exciton–phonon coupling mechanism in these materials. We stress that there is still a lot to be explored in these systems and the investigation of the polarized and resonant properties of the Raman spectra in low-symmetry 2D materials is still only at the beginning stage. For instance, some reports have recently demonstrated the emergence of anisotropic properties in twisted samples of graphene and semiconducting TMDs,[96–101] due to the mismatch between the layers that breaks the axial symmetry. Angle-resolved polarized Raman spectroscopy may provide a new route to study symmetry lowering in twisted 2D structures. Also, the quantification of defects in 2D materials needs attention as it plays a major role in the physical properties of the material. Yu *et al.*[52] reported a study of defects in anisotropic ReS_2 created by argon irradiation and observed the correlation of the defect density and anisotropy. Future studies of defective anisotropic 2D materials may provide new and interesting results. We have only scratched a piece of the quantum formalism to investigate the modulus and phase of the Raman tensor elements and an integration of the Raman tensor expression over all valence and conduction bands and over all wavevectors $\mathbf{k}$ in the Brillouin zone will be needed to fully describe the experimental results. This review demonstrates the importance of angle-resolved polarized Raman spectroscopy to study the fundamental physics of low-symmetry materials, highlighting its uniqueness in the 2D materials field.

Author contributions

The authors researched, collated and wrote the manuscript. The authors discussed and modified the manuscript at all stages.

Conflicts of interest

The authors declare no competing interests.

Acknowledgements

The authors acknowledge the financial support from the Brazilian agencies CNPq, CAPES, FAPEMIG and the Brazilian Institute for Science and Technology of Carbon Nanomaterials (INCT-Nanocarbono).

References

1 K. S. Novoselov, A. K. Geim, S. V. Morozov, D. Jiang, Y. Zhang, S. V. Dubonos, I. V. Grigorieva and A. A. Firsov, *Science*, 2004, **306**(5696), 666–669.
2 K. S. Novoselov, D. Jiang, F. Schedin, T. J. Booth, V. V. Khotkevich, S. V. Morozov and A. K. Geim, *Proc. Natl. Acad. Sci. U. S. A.*, 2005, **102**(30), 10451–10453.
3 M. Chhowalla, H. S. Shin, G. Eda, L.-J. Li, K. P. Loh and H. Zhang, *Nat. Chem.*, 2013, **5**(4), 263.

4 N. Mounet, M. Gibertini, P. Schwaller, D. Campi, A. Merkys, A. Marrazzo, T. Sohier, I. E. Castelli, A. Cepellotti, G. Pizzi and N. Marzari, *Nat. Nanotechnol.*, 2018, **13**(3), 246.
5 S. Zhao, B. Dong, H. Wang, H. Wang, Y. Zhang, Z. V. Han and H. Zhang, *Nanoscale Adv.*, 2020, **2**(1), 109–139.
6 S. Barraza-Lopez, F. Xia, W. Zhu and H. Wang, *Beyond Graphene: Low-Symmetry and Anisotropic 2D Materials*, 2020.
7 J. F. Nye, *Physical properties of crystals: their representation by tensors and matrices*, Oxford University Press, 1985.
8 M. S. Dresselhaus, G. Dresselhaus and A. Jorio, *Group theory*, Springer-Verlag, 1st edn, 2008.
9 M. Tinkham, *Group Theory and Quantum Mechanics*, Courier Corporation, 1st edn, 1992.
10 S. Manzeli, D. Ovchinnikov, D. Pasquier, O. V. Yazyev and A. Kis, *Nat. Rev. Mater.*, 2017, **2**(8), 17033.
11 Z. Lin, B. R. Carvalho, E. Kahn, R. Lv, R. Rao, H. Terrones, M. A. Pimenta and M. Terrones, *2D Mater.*, 2016, **3**(2), 022002.
12 H. Yuan, X. Liu, F. Afshinmanesh, W. Li, G. Xu, J. Sun, B. Lian, A. G. Curto, G. Ye and Y. Hikita, *et al.*, *Nat. Nanotechnol.*, 2015, **10**(8), 707–713.
13 F. Liu, S. Zheng, X. He, A. Chaturvedi, J. He, W. L. Chow, T. R. Mion, X. Wang, J. Zhou and Q. Fu, *et al.*, *Adv. Funct. Mater.*, 2016, **26**(8), 1169–1177.
14 X. Wang, A. M. Jones, K. L. Seyler, V. Tran, Y. Jia, H. Zhao, H. Wang, L. Yang, X. Xu and F. Xia, *Nat. Nanotechnol.*, 2015, **10**, 517.
15 H. Tian, Q. Guo, Y. Xie, H. Zhao, C. Li, J. J. Cha, F. Xia and H. Wang, *Adv. Mater.*, 2016, **28**(25), 4991–4997.
16 H. Wang, M.-L. Chen, M. Zhu, Y. Wang, B. Dong, X. Sun, X. Zhang, S. Cao, X. Li and J. Huang, *et al.*, *Nat. Commun.*, 2019, **10**(1), 1–8.
17 M. N. Ali, J. Xiong, S. Flynn, J. Tao, Q. D. Gibson, L. M. Schoop, T. Liang, N. Haldolaarachchige, M. Hirschberger and N. P. Ong, *et al.*, *Nature*, 2014, **514**(7521), 205–208.
18 A. D. Kent and D. C. Worledge, *Nat. Nanotechnol.*, 2015, **10**(3), 187–191.
19 G. C. Resende, G. A. S. Ribeiro, O. J. Silveira, J. S. Lemos, J. C. Brant, D. Rhodes, L. Balicas, M. Terrones, M. S. C. Mazzoni, C. Fantini, B. R. Carvalho and M. A. Pimenta, *2D Mater.*, 2021, **8**(2), 025002.
20 G. C. Resende, G. A. S. Ribeiro, O. J. Silveira, J. S. Lemos, D. Rhodes, L. Balicas, M. Terrones, M. S. C. Mazzoni, C. Fantini, B. R. Carvalho and M. A. Pimenta, *J. Raman Spectrosc.*, 2021, DOI: 10.1002/jrs.6212.
21 H. B. Ribeiro, M. A. Pimenta, C. J. S. de Matos, R. L. Moreira, A. S. Rodin, J. D. Zapata, E. A. T. de Souza and A. H. C. Neto, *ACS Nano*, 2015, **9**(4), 4270–4276.
22 H. B. Ribeiro, C. E. P. Villegas, D. A. Bahamon, D. Muraca, A. H. C. Neto, E. A. T. de Souza, A. R. Rocha, M. A. Pimenta and C. J. S. de Matos, *Nat. Commun.*, 2016, **7**, 12191.
23 J. B. Renucci, R. N. Tyte and M. Cardona, *Phys. Rev. B: Solid State*, 1975, **11**(10), 3885.
24 M. Cardona, *J. Mol. Struct.*, 1986, **141**, 93–107.
25 F. Widulle, T. Ruf, M. Konuma, I. Silier, M. Cardona, W. Kriegseis and V. I. Ozhogin, *Solid State Commun.*, 2001, **118**(1), 1–22.
26 F. Cerdeira, W. Dreybrodt and M. Cardona, *Solid State Commun.*, 1972, **10**(7), 591–595.
27 B. A. Weinstein and M. Cardona, *Phys. Rev. B: Solid State*, 1973, **7**(6), 2545.
28 J. Menéndez, A. Pinczuk, J. Bevk and J. P. Mannaerts, *J. Vac. Sci. Technol., B*, 1988, **6**(4), 1306–1309.
29 A. Picco, E. Bonera, E. Grilli, M. Guzzi, M. Giarola, G. Mariotto, D. Chrastina and G. Isella, *Phys. Rev. B: Condens. Matter Mater. Phys.*, 2010, **82**(11), 115317.
30 D. Olego and M. Cardona, *Solid State Commun.*, 1981, **39**(10), 1071–1075.
31 G. Burns, F. H. Dacol, C. R. Wie, E. Burstein and M. Cardona, *Solid State Commun.*, 1987, **62**(7), 449–454.
32 J. M. Zhang, T. Ruf, M. Cardona, O. Ambacher, M. Stutzmann, J.-M. Wagner and F. Bechstedt, *Phys. Rev. B: Condens. Matter Mater. Phys.*, 1997, **56**(22), 14399.
33 M. A. Pimenta, E. del Corro, B. R. Carvalho, C. Fantini and L. M. Malard, *Acc. Chem. Res.*, 2015, **48**(1), 41–47.
34 B. R. Carvalho and M. A. Pimenta, *2D Mater.*, 2020, **7**(4), 042001.
35 L. M. Malard, M. A. Pimenta, G. Dresselhaus and M. S. Dresselhaus, *Phys. Rep.*, 2009, **473**(5), 51–87.
36 K. Fujisawa, B. R. Carvalho, T. Zhang, N. Perea-López, Z. Lin, V. Carozo, S. L. L. M. Ramos, E. Kahn, A. Bolotsky, H. Liu, A. L. Elías and M. Terrones, *ACS Nano*, 2021, **15**(6), 9658–9669.
37 B. R. Carvalho, Y. Wang, S. Mignuzzi, D. Roy, M. Terrones, C. Fantini, V. H. Crespi, L. M. Malard and M. A. Pimenta, *Nat. Commun.*, 2017, **8**(1), 1–8.
38 B. R. Carvalho, L. M. Malard, J. M. Alves, C. Fantini and M. A. Pimenta, *Phys. Rev. Lett.*, 2015, **114**, 136403.
39 G. S. N. Eliel, M. V. O. Moutinho, A. C. Gadelha, A. Righi, L. C. Campos, H. B. Ribeiro, P.-W. Chiu, K. Watanabe, T. Taniguchi, P. Puech, M. Paillet, T. Michel, P. Venezuela and M. A. Pimenta, *Nat. Commun.*, 2018, **9**(1), 1221.
40 H. Guo, T. Yang, M. Yamamoto, L. Zhou, R. Ishikawa, K. Ueno, K. Tsukagoshi, Z. Zhang, M. S. Dresselhaus and R. Saito, *Phys. Rev. B: Condens. Matter Mater. Phys.*, 2015, **91**, 205415.
41 P. Soubelet, A. E. Bruchhausen, A. Fainstein, K. Nogajewski and C. Faugeras, *Phys. Rev. B*, 2016, **93**, 155407.
42 T. Strach, J. Brunen, B. Lederle, J. Zegenhagen and M. Cardona, *Phys. Rev. B: Condens. Matter Mater. Phys.*, 1998, **57**, 1292–1297.
43 M. Cardona, *Solid State Commun.*, 1971, **9**(11), 819–822.
44 X. Ling, S. Huang, E. H. Hasdeo, L. Liang, W. M. Parkin, Y. Tatsumi, A. R. T. Nugraha, A. A. Puretzky, P. M. Das, B. G. Sumpter, D. B. Geohegan, J. Kong, R. Saito, M. Drndic, V. Meunier and M. S. Dresselhaus, *Nano Lett.*, 2016, **16**(4), 2260–2267.
45 A.-L. Phaneuf-L'Heureux, A. Favron, J.-F. Germain, P. Lavoie, P. Desjardins, R. Leonelli, R. Martel and S. Francoeur, *Nano Lett.*, 2016, **16**(12), 7761–7767.
46 N. Mao, X. Wang, Y. Lin, B. G. Sumpter, Q. Ji, T. Palacios, S. Huang, V. Meunier, M. S. Dresselhaus, W. A. Tisdale, L. Liang, X. Ling and J. Kong, *J. Am. Chem. Soc.*, 2019, **141**(48), 18994–19001.

47 M.-L. Lin, Y.-C. Leng, X. Cong, D. Meng, J. Wang, X.-L. Li, B. Yu, X.-L. Liu, X.-F. Yu and P.-H. Tan, *Sci. Bull.*, 2020, **65**(22), 1894–1900.
48 Y. Zhu, W. Zheng, W. Wang, S. Zhu, L. Li, L. Cheng, M. Jin, Y. Ding and F. Huang, *PhotoniX*, 2020, **1**(1), 1–9.
49 T. Sriv, T. M. H. Nguyen, Y. Lee, S. Y. Lim, K. Kim, S. Cho and H. Cheong, *et al.*, *Sci. Rep.*, 2020, **10**(1), 1–9.
50 J. Wang, X. Luo, S. Li, I. Verzhbitskiy, W. Zhao, S. Wang, S. Y. Quek and G. Eda, *Adv. Funct. Mater.*, 2017, **27**(14), 1604799.
51 Y. Choi, K. Kim, S. Y. Lim, J. Kim, J. M. Park, J. H. Kim, Z. Lee and H. Cheong, *Nanoscale Horiz.*, 2020, **5**, 308–315.
52 J. Yu, Y. Wang, J. Jiang, Y. Liang, Y. Liu, B. Zhong, S. Quan, M. Zhou, Z. Ni and S. Guo, *Appl. Phys. Lett.*, 2021, **119**(5), 053104.
53 R. Loudon, *Adv. Phys.*, 1964, **13**(52), 423–482.
54 P. Y. Yu and M. Cardona, *Fundamentals of semiconductors*, Springer-Verlag Berlin Heidelberg, 4th edn, 2010.
55 A. C. Albrecht, *J. Chem. Phys.*, 1961, **34**(5), 1476–1484.
56 A. McCreary, J. R. Simpson, Y. Wang, D. Rhodes, K. Fujisawa, L. Balicas, M. Dubey, V. H. Crespi, M. Terrones and A. R. Hight Walker, *Nano Lett.*, 2017, **17**(10), 5897–5907.
57 E. Lorchat, G. Froehlicher and S. Berciaud, *ACS Nano*, 2016, **10**(2), 2752–2760.
58 Q. Song, X. Pan, H. Wang, K. Zhang, Q. Tan, P. Li, Y. Wan, Y. Wang, X. Xu, M. Lin, X. Wan, F. Song and L. Dai, *Sci. Rep.*, 2016, **6**, 29254.
59 R. Beams, L. G. Cançado, S. Krylyuk, I. Kalish, B. Kalanyan, A. K. Singh, K. Choudhary, A. Bruma, P. M. Vora, F. Tavazza, A. V. Davydov and S. J. Stranick, *ACS Nano*, 2016, **10**(10), 9626–9636.
60 C. Kranert, C. Sturm, R. Schmidt-Grund and M. Grundmann, *Phys. Rev. Lett.*, 2016, **116**, 127401.
61 W. L. Peticolas, L. Nafie, P. Stein and B. Fanconi, *J. Chem. Phys.*, 1970, **52**(3), 1576–1584.
62 R. Saito, Y. Tatsumi, S. Huang, X. Ling and M. S. Dresselhaus, *J. Phys.: Condens. Matter*, 2016, **28**(35), 353002.
63 F. Xia, H. Wang and Y. Jia, *Nat. Commun.*, 2014, **5**, 4458.
64 R. Fei, W. Li, J. Li and L. Yang, *Appl. Phys. Lett.*, 2015, **107**(17), 173104.
65 Y. C. Jiang, J. Gao and L. Wang, *Sci. Rep.*, 2016, **6**(1), 19624.
66 K. Zhang, C. Bao, Q. Gu, X. Ren, H. Zhang, K. Deng, Y. Wu, Y. Li, J. Feng and S. Zhou, *Nat. Commun.*, 2016, **7**(1), 1–6.
67 J. Xia, D.-F. Li, J.-D. Zhou, P. Yu, J.-H. Lin, J.-L. Kuo, H.-B. Li, Z. Liu, J.-X. Yan and Z.-X. Shen, *Small*, 2017, **13**(40), 1701887.
68 Q. Song, H. Wang, X. Pan, X. Xu, Y. Wang, Y. Li, F. Song, X. Wan, Y. Ye and L. Dai, *Sci. Rep.*, 2017, **7**(1), 1–10.
69 O. B. Aslan, D. A. Chenet, A. M. Van Der Zande, J. C. Hone and T. F. Heinz, *ACS Photonics*, 2016, **3**(1), 96–101.
70 D. Wolverson, S. Crampin, A. S. Kazemi, A. Ilie and S. J. Bending, *ACS Nano*, 2014, **8**(11), 11154–11164.
71 H. Fujihisa, Y. Akahama, H. Kawamura, Y. Ohishi, Y. Gotoh, H. Yamawaki, M. Sakashita, S. Takeya and K. Honda, *Phys. Rev. Lett.*, 2007, **98**, 175501.
72 L. Li, Y. Yu, G. J. Ye, Q. Ge, X. Ou, H. Wu, D. Feng, X. H. Chen and Y. Zhang, *Nat. Nanotechnol.*, 2014, **9**(5), 372–377.
73 C. A. Vanderborgh and D. Schiferl, *Phys. Rev. B: Condens. Matter Mater. Phys.*, 1989, **40**(14), 9595.
74 A. Brown and S. Rundqvist, *Acta Crystallogr.*, 1965, **19**(4), 684–685.
75 S. Sugai and I. Shirotani, *Solid State Commun.*, 1985, **53**(9), 753–755.
76 D. Çakir, C. Sevik and F. M. Peeters, *Phys. Rev. B: Condens. Matter Mater. Phys.*, 2015, **92**, 165406.
77 R. J. Wu, M. Topsakal, T. Low, M. C. Robbins, N. Haratipour, J. S. Jeong, R. M. Wentzcovitch, S. J. Koester and K. A. Mkhoyan, *J. Vac. Sci. Technol., A*, 2015, **33**(6), 060604.
78 H. Shu, Y. Li, X. Niu and J. Wang, *Phys. Chem. Chem. Phys.*, 2016, **18**(8), 6085–6091.
79 J. Dai and X. C. Zeng, *J. Phys. Chem. Lett.*, 2014, **5**(7), 1289–1293.
80 A. Castellanos-Gomez, L. Vicarelli, E. Prada, J. O. Island, K. L. Narasimha-Acharya, S. I. Blanter, D. J. Groenendijk, M. Buscema, G. A. Steele and J. V. Alvarez, *et al.*, *2D Mater.*, 2014, **1**(2), 025001.
81 J. Ribeiro-Soares, R. M. Almeida, L. G. Cançado, M. S. Dresselhaus and A. Jorio, *Phys. Rev. B: Condens. Matter Mater. Phys.*, 2015, **91**, 205421.
82 X. Ling, L. Liang, S. Huang, A. A. Puretzky, D. B. Geohegan, B. G. Sumpter, J. Kong, V. Meunier and M. S. Dresselhaus, *Nano Lett.*, 2015, **15**(6), 4080–4088.
83 J.-W. Jiang, B.-S. Wang and H. S. Park, *J. Phys.: Condens. Matter*, 2016, **28**(16), 165401.
84 J. Lannin and B. Shanabrook, Physics of Semiconductors, IOP Conf. Proc. Ser., vol. 43, 1979.
85 S. Sugai, T. Ueda and K. Murase, *J. Phys. Soc. Jpn.*, 1981, **50**(10), 3356–3361.
86 S. Liu, N. Huo, S. Gan, Y. Li, Z. Wei, B. Huang, J. Liu, J. Li and H. Chen, *J. Mater. Chem. C*, 2015, **3**(42), 10974–10980.
87 C. Kaneta, H. Katayama-Yoshida and A. Morita, *Solid State Commun.*, 1982, **44**(5), 613–617.
88 J. Kim, J.-U. Lee, J. Lee, H. J. Park, Z. Lee, C. Lee and H. Cheong, *Nanoscale*, 2015, **7**(44), 18708–18715.
89 S.-Y. Chen, T. Goldstein, D. VenkataRaman, A. RamasubRamaniam and J. Yan, *Nano Lett.*, 2016, **16**(9), 5852–5860.
90 J. A. Wilson and A. D. Yoffe, *Adv. Phys.*, 1969, **18**(73), 193–335.
91 L. Hart, S. Dale, S. Hoye, J. L. Webb and D. Wolverson, *Nano Lett.*, 2016, **16**(2), 1381–1386.
92 E. del Corro, H. Terrones, A. Elias, C. Fantini, S. Feng, M. A. Nguyen, T. E. Mallouk, M. Terrones and M. A. Pimenta, *ACS Nano*, 2014, **8**(9), 9629–9635.
93 E. del Corro, A. Botello-Méndez, Y. Gillet, A. L. Elias, H. Terrones, S. Feng, C. Fantini, D. Rhodes, N. Pradhan, L. Balicas, X. Gonze, J.-C. Charlier, M. Terrones and M. A. Pimenta, *Nano Lett.*, 2016, **16**(4), 2363–2368.
94 K. Golasa, M. Grzeszczyk, P. Leszczyński, C. Faugeras, A. A. L. Nicolet, A. Wysmolek, M. Potemski and A. Babiński, *Appl. Phys. Lett.*, 2014, **104**(9), 092106.
95 H. Terrones, E. del Corro, S. Feng, J. M. Poumirol, D. Rhodes, D. Smirnov, N. R. Pradhan, Z. Lin, M. A. T. Nguyen, A. L. Elias, T. E. Mallouk, L. Balicas, M. A. Pimenta and M. Terrones, *Sci. Rep.*, 2014, **4**, 4215.

96 X. Zhang, R. Zhang, Y. Wang, Y. Zhang, T. Jiang, C. Deng, X. Zhang and S. Qin, *Nanotechnology*, 2019, **30**(43), 435702.
97 H. Kim, H. Ko, S. M. Kim and H. Rho, *J. Raman Spectrosc.*, 2020, **51**(5), 774–780.
98 Y. Zhu, W. Zheng, W. Wang, S. Zhu, L. Cheng, L. Li, Z. Lin, Y. Ding, M. Jin and F. Huang, *J. Raman Spectrosc.*, 2020, **51**(8), 1324–1330.
99 M. Jin, W. Zheng, Y. Ding, Y. Zhu, W. Wang and F. Huang, *J. Phys. Chem. Lett.*, 2020, **11**(11), 4311–4316.
100 Y. Ding, W. Zheng, Z. Lin, R. Zhu, M. Jin, Y. Zhu and F. Huang, *Sci. China Mater.*, 2020, **63**, 1848–1854.
101 Y. Ding, W. Zheng, M. Jin, Y. Zhu, R. Zhu, Z. Lin and F. Huang, *Opt. Lett.*, 2020, **45**(6), 1313–1316.